Chapter 9. Laboratory Investigations of the Electromagnetic Properties of Artificial Sea Ice

CALVIN T. SWIFT AND KAREN ST. GERMAIN
Department of Electrical and Computer Engineering, University of Massachusetts, Amherst, Massachusetts 01003

KENNETH C. JEZEK
Byrd Polar Research Center, 1090 Carmack Road, The Ohio State University, Columbus, Ohio 43210

S. PRASAD GOGINENI
Radar Systems and Remote Sensing Laboratory, University of Kansas Center for Research, Inc., 2291 Irving Hill Drive, Campus West, Lawrence, Kansas 66045

ANTHONY J. GOW AND DONALD K. PEROVICH
Cold Regions Research and Engineering Laboratory, 72 Lyme Road, Hanover, New Hampshire 03755

THOMAS C. GRENFELL
Department of Atmospheric Sciences, University of Washington, Seattle, Washington 98195

ROBERT G. ONSTOTT
Environmental Research Institute of Michigan, P. O. Box 8618, Ann Arbor, Michigan 48107

9.1 INTRODUCTION

The electrical properties of sea ice growing on the open ocean are determined by the mechanical and thermodynamical influences of the ocean and atmosphere. Winds, currents, and air and water temperatures, among other variables, contribute to the eventual roughness, texture, chemical composition, and temperature gradient through the sea ice. These latter properties tend to be inhomogeneous over relatively short length scales (tens of meters horizontally and tens of centimeters vertically at best) and they tend to evolve with time as the boundary conditions and internal composition of the ice pack change. For these reasons, the analyses of electromagnetic data collected by spaceborne instruments over sea ice have tended to rely on empirical relationships between limited ranges of an electromagnetic variable (e.g., brightness temperature) and a geophysical property of the ice. Numerous papers document the success of this analysis approach for estimating sea ice concentration and sea ice motion (e.g., Swift and Cavalieri [1985]; Zwally et al. [1983]; Parkinson et al. [1987]). Yet for these same reasons, attempts to obtain a deeper understanding of the electromagnetic properties of naturally growing sea ice can be complicated. For example, it is logistically difficult to measure and sample young sea ice. Some features such as the onset of flooding are transient phenomena, lateral inhomogeneity makes sampling difficult, and the opportunities to view a particular type of ice or even the same piece of ice throughout the seasonal cycle have been rare. Individually, almost all of these problems can and have been overcome by field investigators. But, taken together, there seems to be a strong argument for designing a new approach to answering fundamental questions about sea ice electromagnetic properties, namely, what are the important scattering and absorption mechanisms in sea ice and how are these mechanisms related to ice properties. It was felt that an approach could be found in the laboratory.

The Cold Regions Research and Engineering Laboratory (CRREL) Experiments were designed to confront some of the difficulties encountered in field work by growing sea ice in a carefully constrained, laboratory environment. Microwave experiments were conducted under an overarching set of principles that included: a uniform ice sheet of limited and well-documented physical properties could be grown and maintained; multiple sensors could collect data simultaneously from the same ice; and the interpretation of all electromagnetic observations of the ice with the measured ice physical properties has to be considered. As the experiments progressed, it also became apparent that two more facets needed to be added to the CRREL Experiment (CRRELEX). First, data relevant to a range of electromagnetic models (Chapter 10) needed to be collected. Second, time series data needed to be collected, partly because of initial observations that showed measurable changes in

Microwave Remote Sensing of Sea Ice
Geophysical Monograph 68

electrical properties at every stage of ice development. That CRRELEX could document this evolution is viewed as one of the more important contributions of this work.

9.2 SCOPE

As originally conceived, CRRELEX was designed to study the microwave response of young thin (10 to 20 cm) sea ice that forms on open leads. Facilities were constructed towards this objective and included a saline-water-filled pond fitted with a plastic liner (Figure 9-1). The pond was 12 m long, 5 m wide, and 1 m deep. These dimensions were chosen to accommodate the planned remote sensing instruments. For example, at a width of 5 m, negligible antenna beam spillover occurs at nadir for a C-band radiometer, which has the largest footprint of the remote sensing instruments used. The 12 m length allowed observations at incidence angles up to 50° and provided for acquiring several independent samples with the radars used. An enormous tent could be rolled on and off the pond to protect against changes in weather. Air-conditioning units were installed inside the tent to preserve the ice during inevitable warm temperature periods, but these units were only rarely used and later were abandoned. Paving tiles placed around the perimeter of the pond allowed an instrumented gantry to be moved over the ice. Later, a second, concrete-lined pond 10 m long, 10 m wide, and 1 m deep was outfitted with an instrument shelter, a refurbished movable bridge, and a movable roof. Finally, an indoor test facility used to grow a sea ice simulant from an urea solution and a small refrigerated pit ($8 \times 5 \times 1$ m) were used at the later stages of CRRELEX. The two indoor facilities proved to be extremely valuable in achieving the controlled environmental conditions initially set forth as a CRREL objective. However, the enclosures themselves limited the observations to range-gated radar measurements.

Use of the outdoor facilities placed constraints on the range of simulated ice properties and the duration over which any one ice property could be studied. Thin ice could be grown in an essentially undisturbed fashion for periods of several days. When grown under quiescent conditions, CRRELEX ice sheets exhibited physical properties similar to those found for thin Arctic ice. Depending on whether the ice was seeded with a fine spray of supercooled water or was left undisturbed to develop spontaneously, the upper centimeter of the ice sheet would be composed of smaller or larger

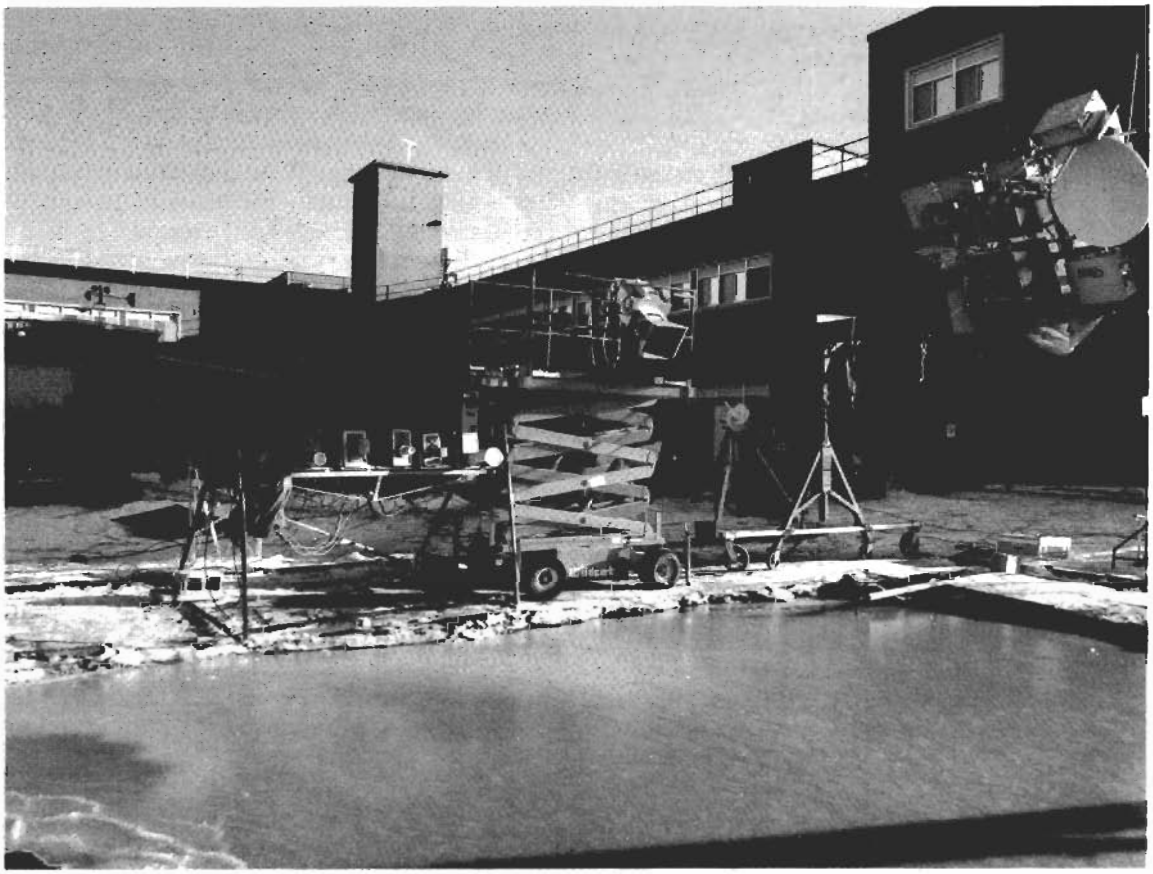

Fig. 9-1. Typical experiment arrangement at the outdoor facility at the Cold Regions Research and Engineering Laboratory. Pictured from the left are five single-frequency radiometers, the Stepped Frequency Microwave Radiometer, and a cluster of radar systems.

crystals with vertical c-axes [Gow, 1986]. A transition in ice properties occurred at a 1 to 2 cm thickness. At that point the c-axes reorient toward the horizontal, and columnar organization of ice crystals, characteristic of Arctic congelation ice, becomes dominant (Figure 9-2).

Congelation ice sheets were routinely grown during CRRELEX with maximum thicknesses ranging from about 10 to 30 cm, depending on the experimental requirements. In each case, the ice was closely monitored for salinity, crystal structure, brine pocket distribution, and, as possible, surface roughness. An example of the structural and salinity characteristics of an ice sheet monitored from initial growth to decay is presented in Figure 9-3. In this particular case, ice growth was initiated in January 1985, and for the first month this ice sheet exhibited typical C-shaped salinity profiles, Figure 9-4(a). Subsequent pooling of snow melt and rain on top of the ice sheet in late February to early March 1985 led to significant downward percolation of the water and concomitant desalination of the ice before the pooled water refroze to produce the salinity and structural characteristics of ice depicted in Figure 9-3. At this stage, the ice contained few brine inclusions and the outlines of crystals had become rounded, a situation similar to multiyear Arctic ice [Gow et al., 1987].

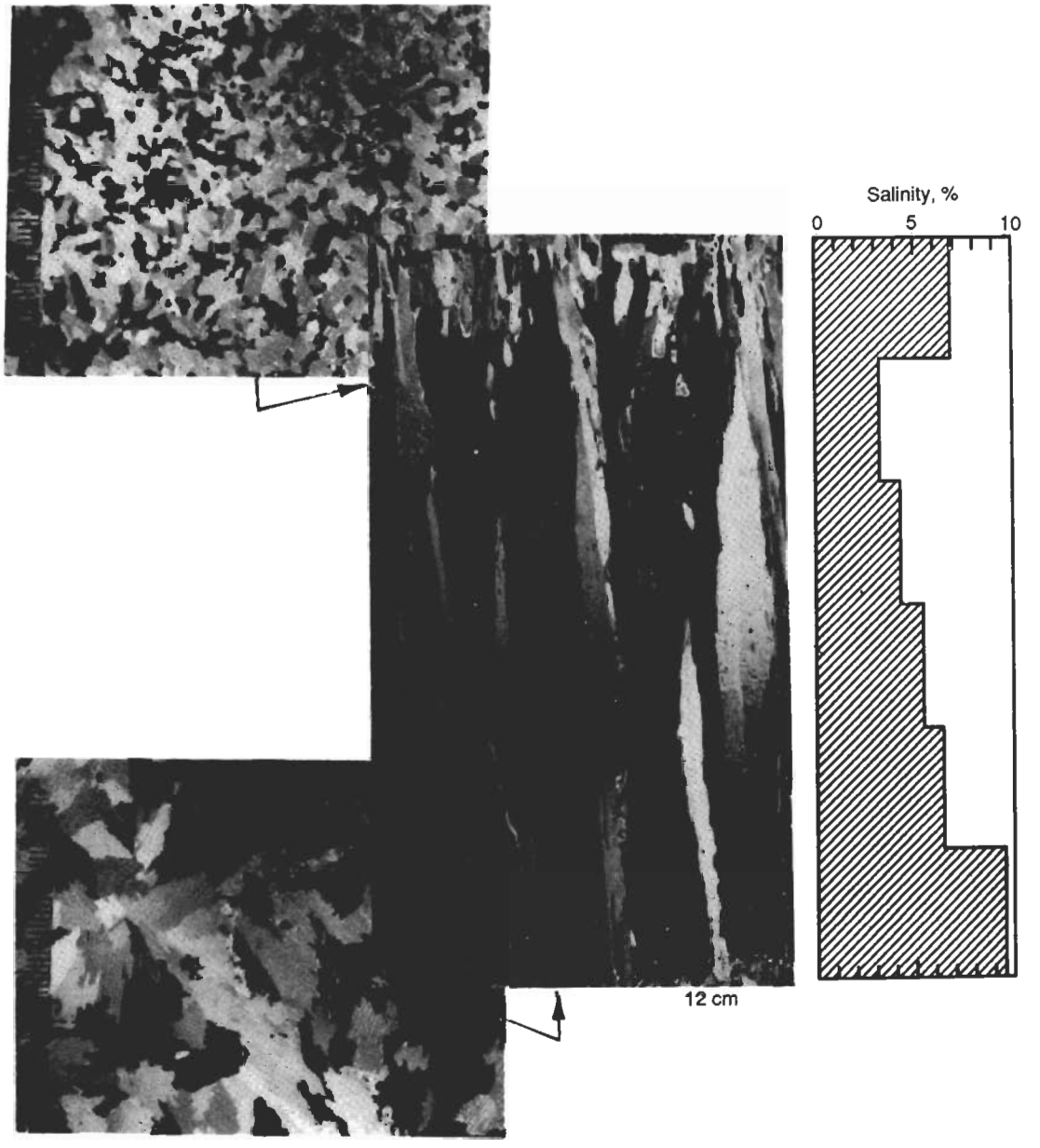

Fig. 9-2. The ice shown in these vertical and horizontal thin-section photographs and salinity profile is freshly grown saline ice from the CRREL test pond. Structurally, this ice closely simulates young Arctic sea ice. Scale subdivisions in horizontal sections measure 1 mm.

Salinity profiles documenting the progressive desalination of the January to March 1985 CRRELEX saline ice sheet are shown in Figure 9-4(b). Desalinated ice was also produced by cutting a pre-existing ice sheet into blocks and placing the blocks on wooden pallets. The blocks were allowed to weather and desalinate under ambient conditions. At the end of this process, the blocks were overlain on a second ice sheet growing in the pond; block salinities did not exceed 0.35‰.

Figure 9-5 documents salinity, temperature, brine volume, and crystalline structure more typical of 10 to 15 cm thick congelation ice sheets grown on the outdoor ponds at CRREL. Temperatures increase linearly with depth. Brine volumes are nearly constant (about 3%) in the upper 75% of the ice. Below that level, brine volumes increase rapidly in the region where the ice develops a more open dendritic structure. A characteristic C-shaped salinity profile is found in this ice with a maximum value at the surface of about 8‰ (averaged over three cm) and a minimum of 5.4‰ at a depth of 10 cm. Salinity increases below 10 cm again because of the structure of the dendritic layer. The horizontal distribution of brine pockets was quantified by digitizing horizontal thin sections taken at various levels through the ice sheet.

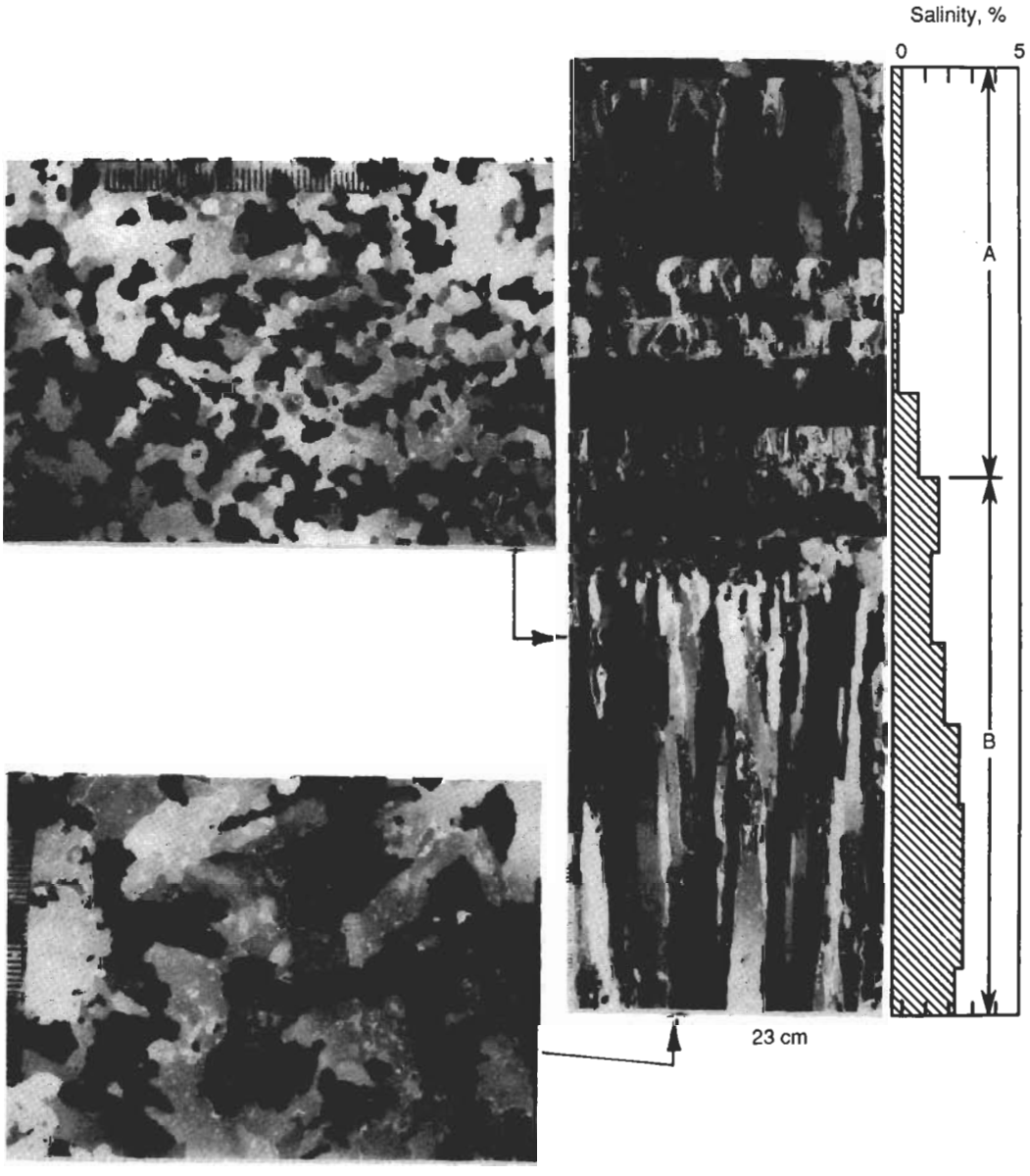

Fig. 9-3. Crystalline structure and salinity characteristics of ice desalinating in the CRREL test pond. In this example, several layers of melt pond ice (A) overlie desalinated columnar saline ice (B). Scale subdivisions in horizontal sections measure 1 mm.

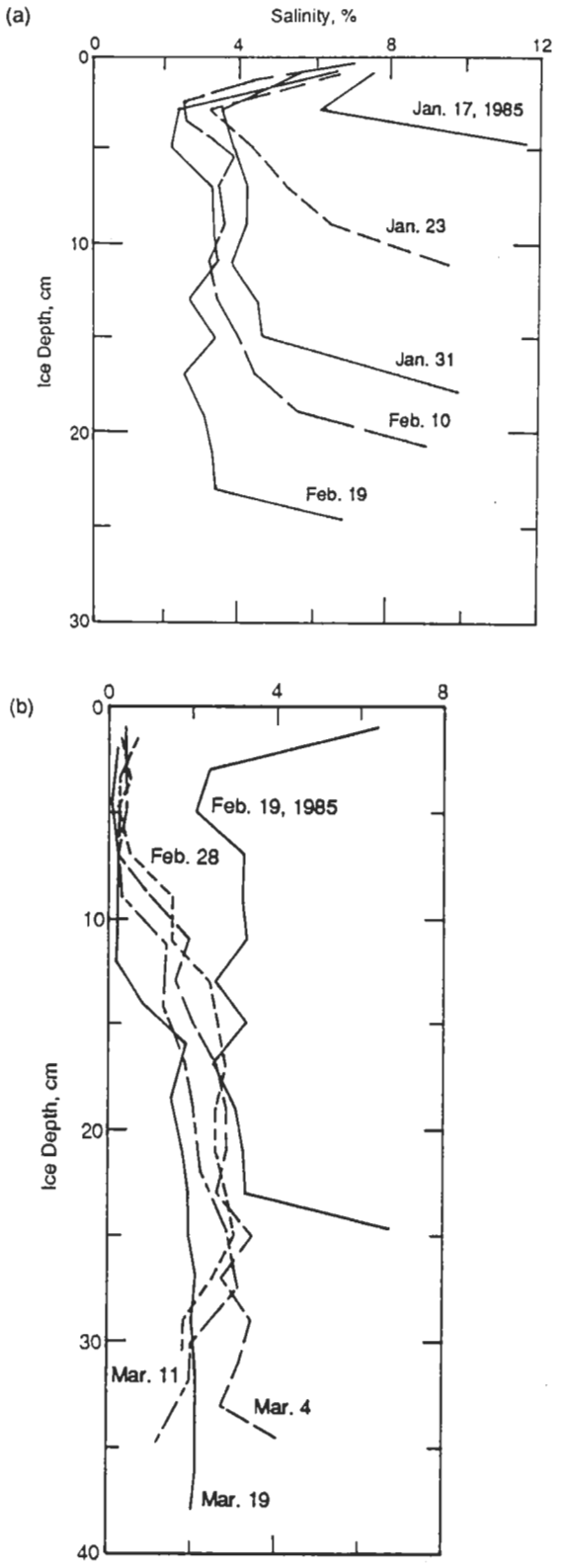

Fig. 9-4. (a) Salinity profiles at different stages of growth of sea ice grown in an outdoor pond at CRREL. Profiles closely simulate those found in Arctic first-year ice. (b) Transformation from a new ice to desalinated ice salinity profile in the outdoor pool at CRREL.

With additional experimentation, it was found that several other physical properties and ice-growth processes could be simulated in the laboratory. Varying surface roughness was introduced either by manually raking the ice surface or by spreading a layer of small chunks of ice on the growing ice sheet. In a few instances, larger blocks of ice were assembled into simulations of ridges. Other classes of complementary experiments could be included during each CRRELEX, and high-frequency acoustic [Stanton et al., 1986; Jezek et al., 1990] and optical frequency propagation measurements were often conducted simultaneously with the microwave observations.

Frazil ice, which forms in turbulent seas and has a granular texture, was simulated in three different ways. Snowfall onto the surface of the unfrozen pool produced a slush cover. Frozen slush results in an ice cover with salinity and structural characteristics very similar to frazil ice. Granular, frazil-like ice sheets up to 8 cm thick were produced in this manner. The second method for producing frazil ice involved a submersible pump to induce frazil crystal nucleation in the pool and the herding of crystals into a layer up to 4 cm thick. A third method simulated both frazil production and the agglomeration of frazil platelets into pancake ice. Here a wave generator consisting of a motor-driven panel was positioned at one end of the pond. Turbulence and wave action converted the semiconsolidated frazil ice sheet into a field of pancakes with pans measuring 20 to 30 cm in diameter and several centimeters thick. The vertical structure of a typical pancake including a salinity profile is presented in Figure 9-6.

Snow-covered ice was studied on the outdoor ponds and also under more controlled conditions in the indoor pit. Analyses of snow-covered ice is complicated by the subtle modification of the ice–snow surface when thin layers of snow are applied. A snow layer is absorbent and, over time, tends to wick surface brine up into the snow layer. This process seems to result in a dielectric roughening of the interface, although direct measurements of the amount or degree of roughening have yet to be made. A sufficient snow load will depress the ice surface below the unloaded freeboard, causing the surface to flood. Flooding was studied in the laboratory by loading a slab of ice with snow and then cutting the slab free from the restraining walls of the tank.

Finally, it is worth mentioning that frost flowers routinely developed in the indoor test basin and cold pit. Preliminary radar measurements were made on freshwater ice sheets completely covered by frost flowers and on urea and saline ice sheets with a low density of frost flowers.

As mentioned, many of the early CRRELEX's were exercises in learning about the ice. As each experiment was completed, it seemed possible to more clearly articulate several questions that drove the development of subsequent experiments:

- What are the microwave absorption and scattering coefficients of thin sea ice? How do they change with time?

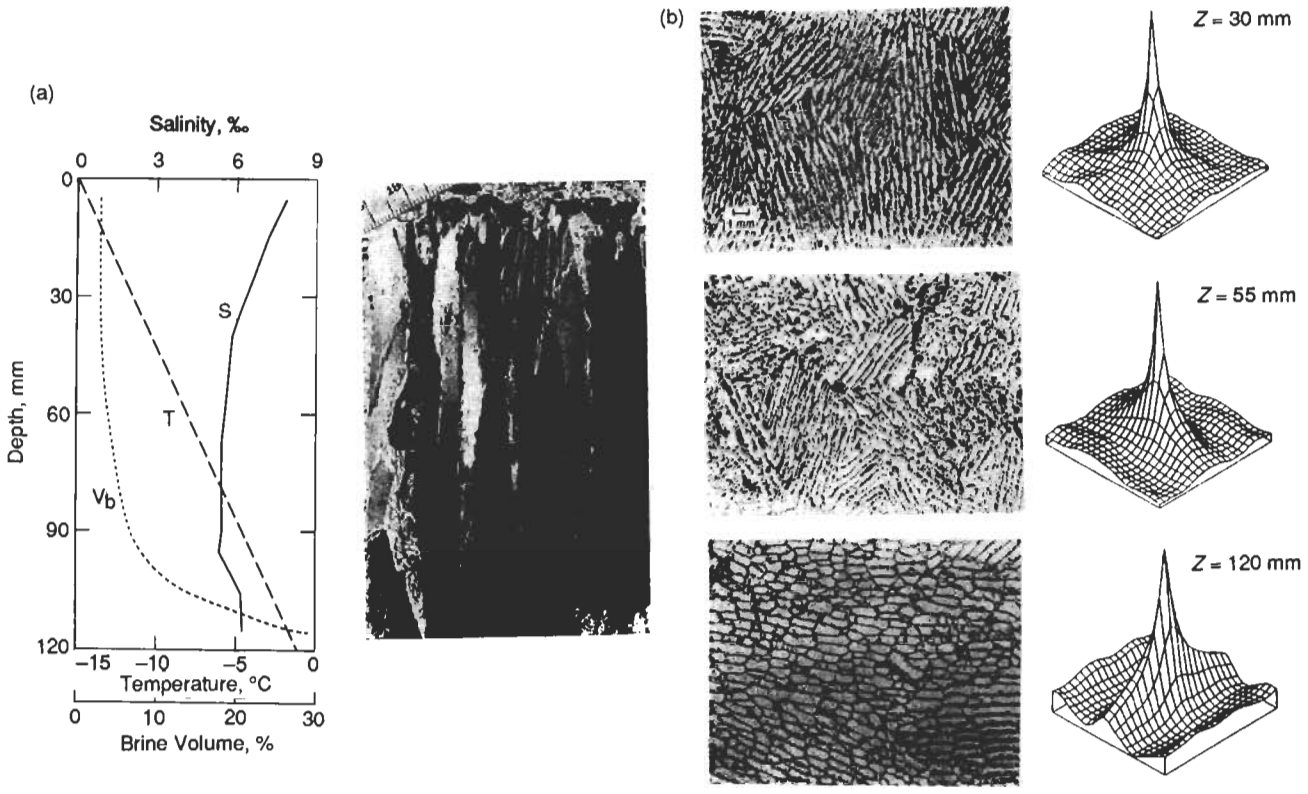

Fig. 9-5. Vertical profiles of temperature (T), salinity (S), and brine volume (V_b) for young sea ice. The vertical thin section shows that the ice structure is predominantly columnar with a thin surface layer of frazil. Also shown are horizontal thin sections from the top, middle, and bottom of the ice sheet with corresponding correlation functions [Perovich and Gow, 1991].

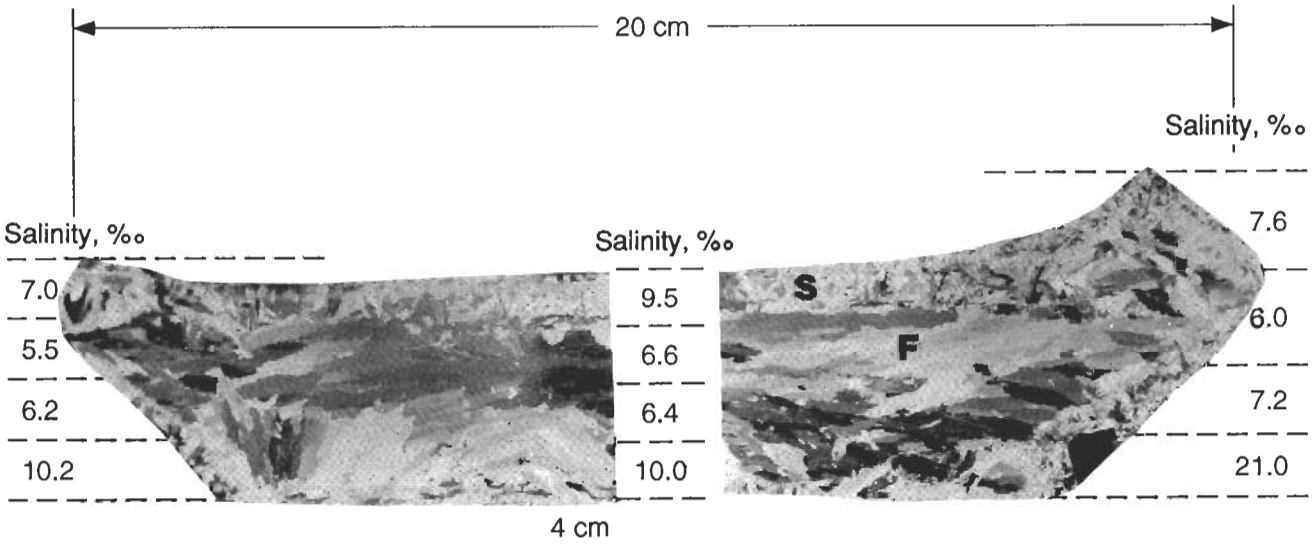

Fig. 9-6. Vertical thin-section structure and salinity profiles from a 4 cm thick pancake from CRRELEX'90. The sequence of ice textures from top to bottom of the pan is slush ice (s) underlain by platey frazil ice (f).

- To what thickness and in what fashion does the ice–water interface and the dendritic layer control electromagnetic response at a particular frequency?
- How important are the shapes, orientation, density, and distribution of brine pockets on the microwave response?
- Given that different classes of surface roughness are associated with different ice formation scenarios, which are the most important roughness classes; which classes dominate over, are equivalent to, or are less than volume scatter effects? Does the sequence of steps in the development and destruction of particular morphologies (e.g., frost flowers) result in a characteristic sequence of microwave responses?
- Does snow play a role in coupling electromagnetic energy between the air, snow, and ice? Is the modification of the ice surface due to the presence of thin snow an important effect? What happens to electromagnetic signatures when snow is sufficiently thick to cause flooding?
- Do thin ice, snow-covered ice, deformed ice, and ridges display azimuthal electromagnetic response? If so, why?
- How and why do signatures change when thin ice warms and desalinates and how is this related to the changing internal structure of the ice?

9.3 Growth Phase of Thin Saline Ice

Microwave backscatter, transmission, and brightness temperature measurements were made by the CRRELEX team on saline ice during the winters from 1984 to 1989. Results from all measurements on undeformed congelation ice are similar. Results of representative experiments from this period are used to illustrate the range of measured responses.

Figure 9-7 shows the variation with time of the backscatter coefficient at 5.3 GHz as the surface evolves from open water to grey ice (14.5 cm thick) [Gogineni et al., 1990].

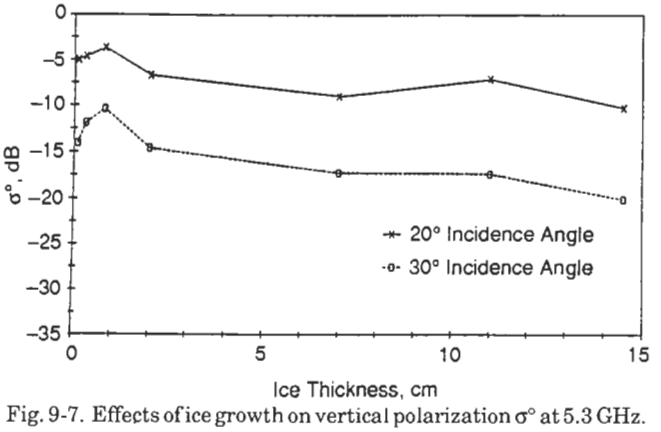

Fig. 9-7. Effects of ice growth on vertical polarization σ° at 5.3 GHz.

Vertically polarized data from 1984 are shown at 20° and 30° angles of incidence. For ice thicknesses greater than 3 cm, the scattering coefficients remained nearly constant, and possibly decreased when the ice thickness exceeded 12 cm. A more complicated response was observed for very thin ice during the transition from horizontal to vertical crystallographic orientation. The scattering coefficient increased immediately subsequent to ice formation, reached a maximum value at about 1 cm thickness, and then decreased, reaching a stable value after about 2 cm of growth. A similar behavior has been observed for measurements performed at 13.9 GHz on an ice sheet growing from an urea solution in the laboratory. Two mechanisms may contribute to the thin ice response: a high surface dielectric constant and surface roughening (e.g., frost flowers). Frost flowers or other macroscopic surface phenomena were not observed during the experiment. Although surface roughness changes cannot be ruled out on the basis of available observations, it seems more probable that a high dielectric constant explains the data. During initial ice growth, brine is expelled onto the ice surface and surface salinities as large as 70‰ have been reported [A. Kovacs, personal communication, CRREL, Hanover, New Hampshire, 1988].

Figures 9-8, 9-9, 9-10, and 9-11 show both the changing microwave signatures and the changing physical properties of the ice sheet for the 1985 experiments [Onstott, 1991]. Data were obtained at several frequencies and are shown at both like polarizations and at 0° and 40° angles of incidence. Two responses from open water were measured: at the beginning of the growth cycle with small ripples present and a rippleless case at the end of the growth cycle. Both open water points appear at the beginning of the time series.

In this experiment, at an oblique incidence angle (Figure 9-8), there is no evidence of a rise or fall in the thin ice backscatter response, though there is a weak suggestion of

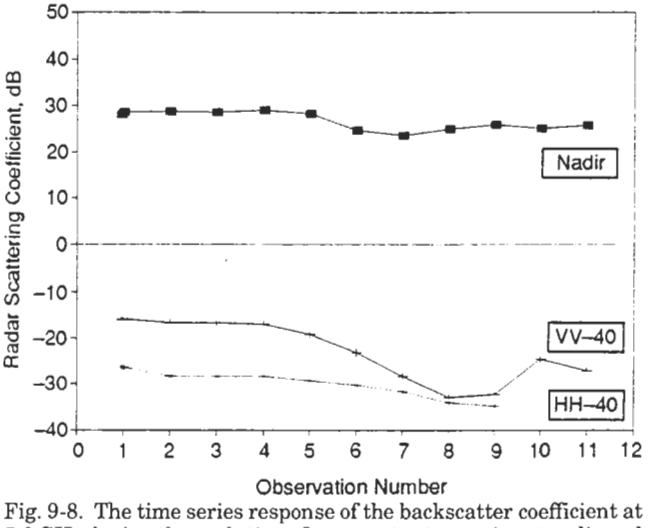

Fig. 9-8. The time series response of the backscatter coefficient at 5.0 GHz during the evolution of open water to new ice at nadir and 40° (VV and HH).

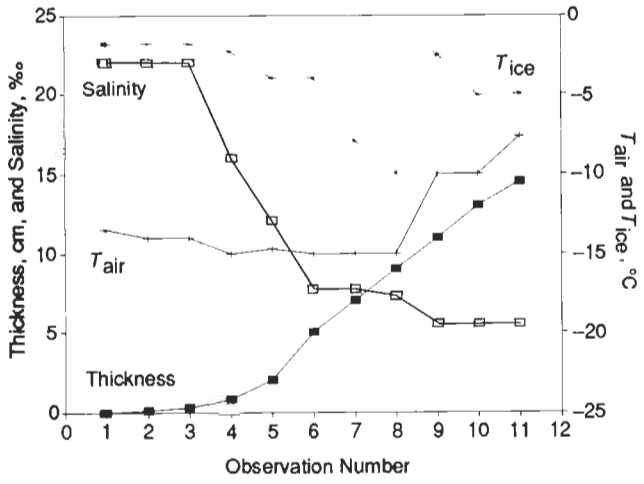

Fig. 9-9. Ice thickness, air temperature, ice temperature, and bulk salinity during the evolution of open water to new ice.

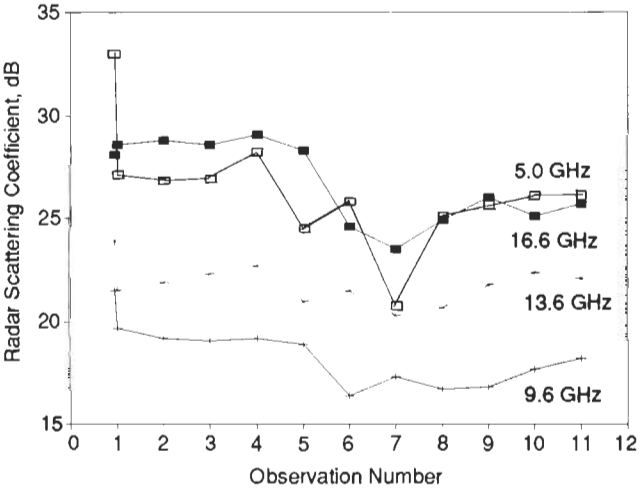

Fig. 9-10. The time series response of backscatter at vertical incidence during the evolution from open water to new ice shown as a function of frequency from 5.0 to 16.6 GHz.

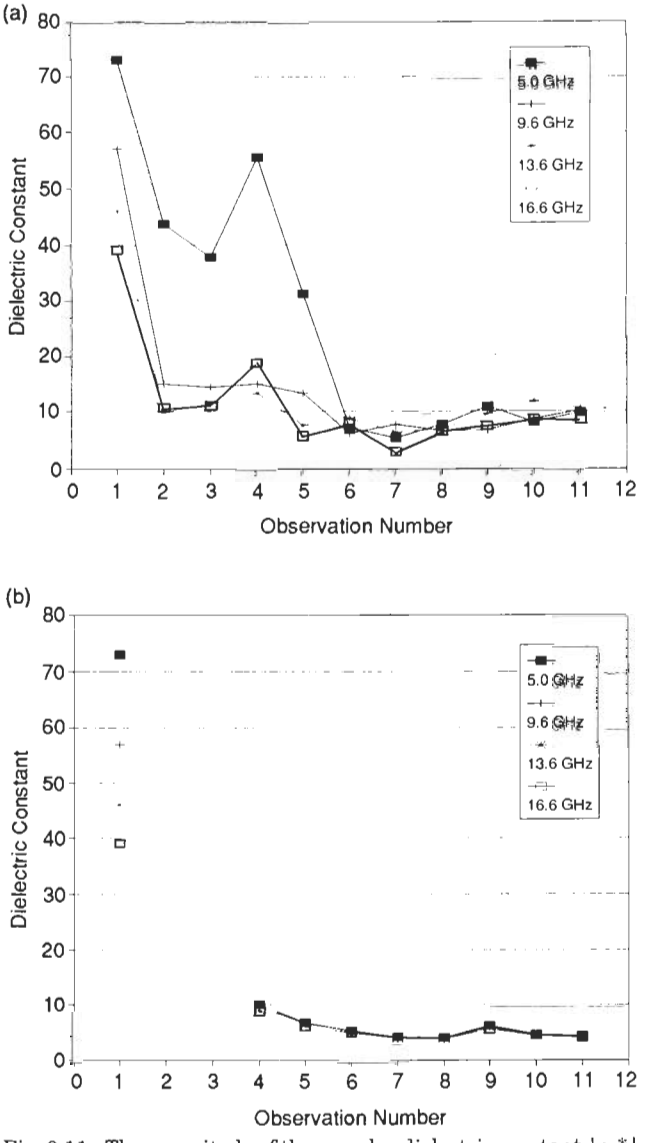

Fig. 9-11. The magnitude of the complex dielectric constant $|e_r^*|$ (a) as derived from the measurement of reflectivity and (b) by prediction.

that phenomenon at normal incidence angles (Figure 9-10). The backscatter is relatively constant (a slope of 0.05 with a mean square error of 0.4 dB) in the ice thickness range from 0 to 2 cm. Immediately subsequent to formation, the ice was very smooth visually, and measurements made later in the experiment indicated roughnesses of 0.05 cm root mean square (rms) with typical correlation lengths of 1 to 2 cm. The magnitude of the complex dielectric constant calculated from the scattering coefficient at nadir and at 5 GHz is (assuming a smooth surface) 42 ±9 (Figure 9-11). This high value for the dielectric constant is consistent with the inferences made from the data in Figure 9-7.

Near-surface ice temperatures and bulk salinities decreased as the ice thickened. A change in both ice physical properties and microwave properties is evident at about OB5. The crystallographic orientation and growth process has undergone a transformation at this point. Evidently, the change in bulk properties and processes is driving a change in the electromagnetic response.

Even under relatively controlled conditions, the ice sheet surface will undergo a metamorphosis with time. Single snow particles blown onto the ice sheet (OB8–OB11) increase the roughness of new ice by creating an "orange peel" surface. Onstott [1991] observed that when snow particles are deposited onto new ice, brine is wicked from the ice layer and deposited about the snow particles. The particles melt, dilute the brine solution, and then refreeze. This process creates small roughness elements that modify the backscat-

ter response. Bredow [1991] also investigated the relative contributions of volume scattering from brine pockets and scattering from the surface of thin saline ice. Modeled and predicted variations of X-band backscatter strength with incidence angle agreed well with a Kirchoff scattering model. Bredow also compared the measured radar pulse shape with simulations and found that the pulse shapes were primarily governed by surface scatter along with a weak volume scatter component that caused a slight broadening of the received pulse. At C-band, Bredow found that volume and surface scattering contribute about equally to the ice signature, presumably because of increasing penetration depth.

Linearly polarized radiometers operating at 10, 18, 37, and 90 GHz were used to observe the changing brightness temperature during the growth phase of thin ice. The variation in ice emissivity versus thickness during the growth phase is shown in Figure 9-12 for frequencies of 18, 37, and 90 GHz. The signature is characterized by a rapid increase in emissivity with increasing ice thickness up to a saturation level. Similar results at 10, 18, 37, and 90 GHz, vertical polarization and 50° incidence angle, are reported by Grenfell and Comiso [1986]. They show that emissivity increased from 0.525 to 0.95 at 10 GHz during the initial 50 mm of growth. They also found that emissivity at higher frequencies increased more rapidly with increasing ice thickness.

Results of concurrent radiometer measurements taken at C-band are shown in Figures 9-13 and 9-14. As expected, the emissivity at C-band saturates at substantially thicker ice than would be the case for higher frequencies. As discussed in the next section, the general shape of the curve is as would be predicted by a model that only allows for the incoherent addition of energy propagating through the ice. However, the excursion observed during the initial growth phase is undoubtedly a coherent effect associated with the first half of an interference fringe. Figure 9-14 demonstrates that a change in wavelength influences the periodicity of the first minimum.

Grenfell and Comiso [1986] compare the degree of polarization P (defined as the ratio of the difference between the

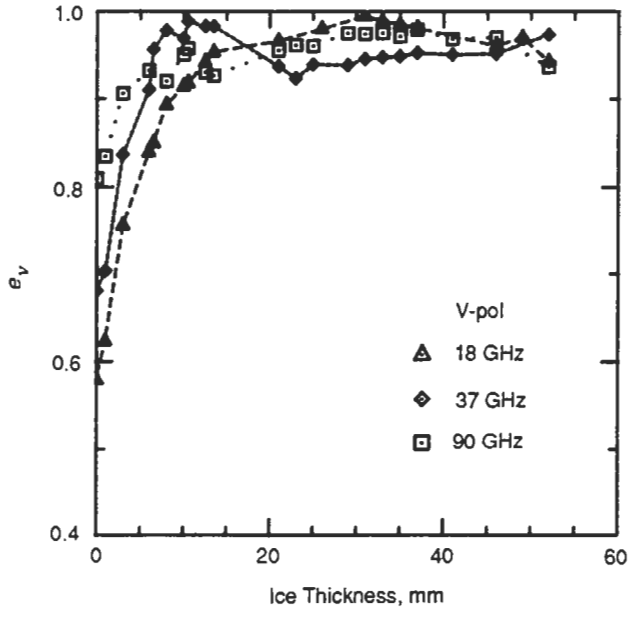

Fig. 9-12. Ice emissivity versus thickness for 18-, 37-, and 90-GHz vertical polarizations during initial growth of congelation ice [Grenfell et al., 1988].

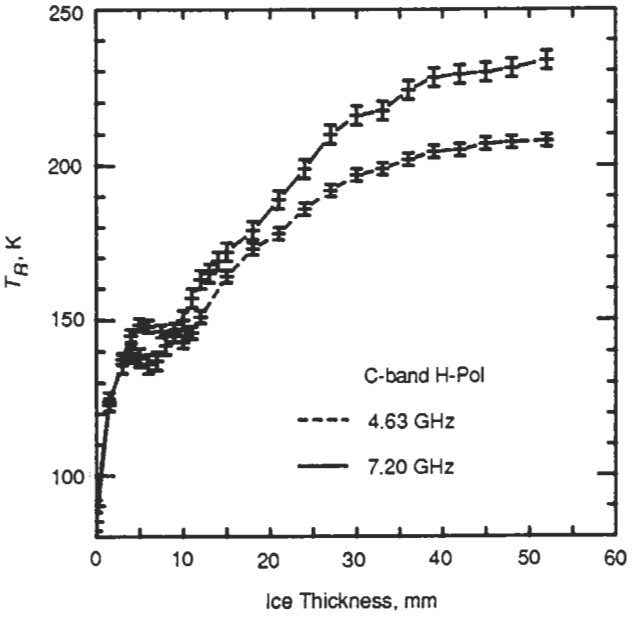

Fig. 9-13. Brightness temperature versus thickness during initial growth at two C-band frequencies and horizontal polarization. These observations cover the same ice sheet as in Figure 9-12 [Grenfell et al., 1988].

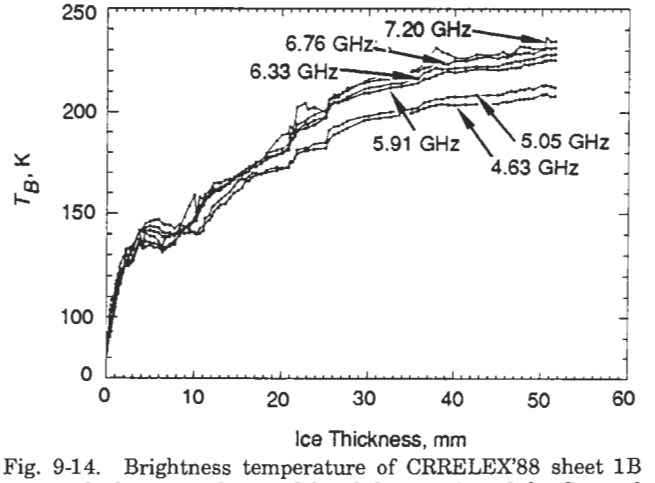

Fig. 9-14. Brightness temperature of CRRELEX'88 sheet 1B versus thickness at the six C-band frequencies of the Stepped Frequency Microwave Radiometer. The measurements were taken at horizontal polarization and a 35° incidence angle. Data from Figure 9-13 are included here without the associated uncertainty bars.

two linear polarizations divided by their sum at a single frequency), during the early growth stages. Polarization decreased by about 60% at 18 GHz as the ice grew to a thickness of about 20 to 25 mm—somewhat less than was required for the emissivity to reach a comparable saturation level.

Arcone et al. [1986] discussed a series of transmission measurements on ice samples extracted from the CRREL pond, as well as in-situ observations acquired by placing antennas above the slab and in the water below the ice slab. Data were evaluated to estimate real and imaginary parts of the dielectric constant. Each experiment required that the ice maintain mechanical integrity and hence the minimum ice thickness sampled was about 7 cm, for which a well-ordered columnar structure was established. Slabs removed from the pond to a refrigerated laboratory were subjected to cyclic cooling and warming.

Loss was measured in situ at 4.5, 4.8, 8.9, 9.0, 9.15, and 10 GHz and was found to vary between 4.1 and 8.7 dB/cm. Higher loss rates were associated with higher frequencies. The highest loss rates were also associated with the thinnest ice. Such ice would be relatively warm and hence would have the highest brine volume fraction. Arcone et al. [1986] reported real permittivities for samples removed from the pond. Values ranged from a maximum of about 4.5 for a slab temperature of –4°C to about 3.2 for cold slabs. The authors modeled the permittivity of high salinity thin ice and concluded that the real part varied from about 10 to about 4 for the temperature range –2° to –10°C in the frequency range 4.8 to 9.5 GHz. In general, Arcone et al. found that both the real and imaginary parts varied linearly with brine volume.

9.3.1 Thin Ice Data Interpretation

Variations in radar backscatter and microwave emission data during thin ice growth seem to be associated with a transition in ice physical properties. The onset of freezing is characterized by the formation of a thin skim of ice that quickly evolves into a complex of stellar crystals. The optical axis of these ice crystals is horizontal, their crystalline texture looks granular in vertical cross section, and brine is expelled onto the ice surface. This upper, transitional layer of thin ice tends to be brine-free and bubble-free. After 1 or 2 cm of growth, a columnar structure develops wherein brine is expelled downward or is trapped within isolated pockets.

These evolving ice processes force progressive changes in the ice sheet's electrical properties. In particular, Figure 9-11 shows that very new sea ice has a dielectric constant much smaller (about 75%) than that of open water. Between thicknesses of 1 and 2 cm, the dielectric constant reaches a maximum value. Consequently, the backscatter response at normal incidence increases with the largest changes at higher frequencies (Figure 9-10). These radar observations are consistent with the facts that: brine is gradually being expelled to the surface as the freezing process progresses; brine accumulation peaks (in this study at 1 cm ice thickness); and a large percentage change in the dielectric constant occurs.

At 2 cm thickness (OB5), Figure 9-8, backscatter response for VV-40 decreased significantly while the backscatter at nadir remained within about 1 dB. This indicates that multiple processes were at work. The nadir response at 5 GHz directly tracked the change in dielectric constant, while the responses at oblique incidence were sensitive to both the change in dielectric constant and changes in surface roughness statistics.

After the ice is about 2 cm thick, growth proceeds by the accretion of ice to the base of columnar crystals. Based on the normal incidence backscatter data, the magnitude of the dielectric constant after columnar growth is initiated was about 7 (OB6 in Figure 9-11) and reached a minimum about 6 hours later [Onstott, 1991]. The surface roughness at this point was 0.05 cm rms and the ice surface temperature had cooled to –4°C. By accounting for the change in the dielectric constant between the transitional ice growth phase and columnar growth, the roughness for the initial skim was determined to be about 0.065 cm rms. This estimate was based on predictions using the small perturbation model.

As ice growth continues, ice nearest the surface cools and the surface brine layer dissipates. The thickening layer of highly emissive ice shields the radiometrically colder water. This causes brightness temperatures to elevate at a rate proportional to their frequency. Dissipation of the thin, highly concentrated brine layer at the surface of the ice sheet will result in an additional emissivity increase. Also, as Arcone et al. [1986] pointed out, lower temperatures decrease the bulk dielectric constant, which in turn causes a decrease in the backscatter response. Figure 9-10 reveals a 7.5-dB reduction in backscatter (5.0 GHz and VV) between ice 0 to 1 cm thick and ice 4 to 7 cm thick.

To examine the frequency dependence during the transition to a columnar ice structure, the average value of the dielectric constant for OB1 through OB5 and the minimum value measured immediately at the beginning of columnar growth are used, Figure 9-11(a). Associated changes in backscatter are 5, 3, 2, and 2 dB at 5.0, 9.6, 13.6, and 16.6 GHz, respectively. Since cooling is a top-down process, changes at higher frequencies are expected to occur first. This is verified by correlating the physical observations in Figure 9-9 with the reflectivity response at ice thicknesses between 0 and 2 cm. The time at which the drop in dielectric constant occurs is frequency dependent. This level was reached at a thickness of 5 cm (OB6) for 5.0 and 9.6 GHz, and 2 cm (OB5) for 13.6 and 16.6 GHz. This trend further illustrates that the magnitude of the backscatter response is driven by the dielectric constant and that an effective bulk dielectric constant is determined by penetration depth, both of which are frequency dependent.

A modified version of a model developed by Kovacs et al. [1986] was used to predict dielectric profiles so that penetration depths and bulk dielectric constants could be calculated at each frequency. For comparison, these results are included in Figure 9-11(b). The C-shaped salinity

profile further modulated the effective dielectric constant, especially at high frequencies, because of an increase in the brine volume in the uppermost portion of the ice sheet. Examination of the penetration depths provided in Table 9-1 shows that the backscatter response at 5.0 GHz was influenced by the entire dielectric layer for thicknesses from 0 to 2 cm. In contrast, at 16.6 GHz, the top 0.5 cm sets the absolute level of the backscatter response.

New ice grown under very calm conditions has a very smooth ice–air interface; however, the surface may become slightly roughened with the deposition of single snow crystals. This observation and Bredow's [1991] result at C-band that volume and surface scattering contribute about equally to the ice signature for very smooth ice argue that backscatter data at C-band and higher frequencies provide information about the upper layers of the ice. Radiometric results presented in Figures 9-12, 9-13, and 9-14 argue that at C-band frequencies and lower, brightness temperature data represent an integration of effects distributed throughout the thin ice sheet. In particular, Figure 9-14 shows an oscillatory dependence of brightness temperature of young sea ice with frequency and ice thickness. This dependence indicates that microwave emission from young sea ice also includes a coherent process.

Apinis and Peake [1976] derive an expression for coherent emission from a slab:

$$\varepsilon = 1 - r = \frac{(1 - r_i)(1 - Ar_w)}{(1 + Ar_i r_w + 2\sqrt{Ar_i r_w}\cos 2B\ell)} \qquad (1)$$

where r is the composite power reflection coefficient
r_i is the power reflection coefficient at the air–ice interface
r_w is the power reflection coefficient at the ice–water interface
$A = \exp(-4\alpha\ell)$
α is the attenuation coefficient in ice
B is the phase constant in ice
ℓ is the radiation path length

This expression shows that the emissivity is a damped, periodic function of ice thickness. Of course, interface roughness will destroy coherence and, if the surface is sufficiently rough, the average emissivity is given by

TABLE 9-1. Predicted penetration depths for sea ice with thicknesses from 1 to 8 cm [Onstott, 1991].

Ice thickness,	Penetration depth, cm, for given frequencies			
cm	5.25 GHz	9.6 GHz	13.6 GHz	16.6 GHz
1	>1	0.8	0.5	0.4
2	2.0	1.0	0.7	0.5
4	3.3	1.6	1.0	0.8
8	3.7	1.6	1.0	0.8

$$\langle \varepsilon \rangle \simeq \frac{(1 - r_i)(1 - Ar_w)}{(1 - Ar_i r_w)} \qquad (2)$$

This very simple expression depends only on the reflection coefficients at the two interfaces and the product of the attenuation coefficient and path length. Therefore, if the bulk electrical properties are known, the total incoherent emissivity is a function only of the slab's mean thickness. The monotonic increase in emissivity predicted by Equation (2) is supported by data for ice with significant surface roughness [Swift et al., 1986]. (Equation (2) does not reduce to the proper value for zero slab thickness. An empirical equation has been introduced by Swift et al. [1986] to correct this limitation.)

Variations in emissivity shown in Figures 9-12 and 9-14 can be understood in terms of incoherent and coherent processes. The signatures in Figure 9-12 are characterized by rapid increases in emissivity with increasing ice thickness up to a saturation level—this is the functional form predicted by the incoherent propagation model. The frequency, ice thickness, and ice extinction coefficients will determine when the saturation level will be reached. To show this relationship more clearly, the attenuation coefficient, A, can be expressed as

$$A = e^{-4\alpha d_0} = \exp\left(\frac{-8\pi n_i d_0}{\lambda_0}\right) \qquad (3)$$

where n_i is the imaginary part of the refraction index of sea ice. Because n_i is expected to be reasonably constant over the microwave band of frequencies, Equation (3) shows that the attenuation increases as the frequency of observation increases. This result agrees with the data trends in Figure 9-12, which indicate that for a given ice thickness, the emission from the underlying water decreases as the operating frequency increases.

The results of concurrent measurements taken at C-band are shown in Figure 9-14. Since the C-band wavelength is much larger, saturation is reached at substantially thicker ice. This signature is very similar to that predicted by the incoherent model, except for the excursion noted during the initial growth phase. This is undoubtedly a coherent effect associated with the first half-wave interference fringe. The interference patterns at 4.63 and 7.20 GHz are distinct. From Equation (1), we expect to observe a maximum when $l/\lambda_i = 0.25$ and a first minima at $l/\lambda_i = 0.5$.

Because the ice thickness was frequently measured, the data can be used to solve for the average dielectric constant of the ice layers. St. Germain and coworkers [St. Germain, K. M., C. T. Swift, and T. C. Grenfell, Determination of dielectric constant of young sea ice using microwave spectral radiometry, submitted to the *Journal of Geophysical Research*] derived a relationship between the real part of the dielectric permittivity and ice thickness given by

$$\varepsilon_r' = \frac{1}{2}\left\{\left(\frac{c\ell}{d_0 f\,\lambda_i}\right)^2 \pm \sqrt{\left(\frac{c\ell}{d_0 f\,\lambda_i}\right)^4 - 4\left(\frac{c\ell}{d_0 f\,\lambda_i}\right)^2 \sin^2\theta_i}\right\} \quad (4)$$

Table 9-2 presents a listing of thicknesses that correspond to the first and second quarter-wave interference fringes. Using data from Table 9-2 along with Equation (4) allows one to solve for the dielectric constant of ice. Results are presented in Figure 9-15, where a linear regression has been plotted through the data points. This figure shows that the dielectric constant of ice during the first centimeter of growth is approximately three times larger than results quoted for thick first-year ice, which is consistent with results reported above. St. Germain and coworkers evaluated the frequency dependence of the dielectric constant and found that n_i is equal to about 0.038 ($\varepsilon = 0.215$).

TABLE 9-2. Mean ice thicknesses measured at the first maximum $d/\lambda = 0.25$ and the first minimum $d/\lambda = 0.50$ in the time series brightness temperature data for each frequency.

Frequency, GHz	d_0 [$d = \lambda/4$], mm	d_0 [$d = \lambda/2$], mm
4.63	5.0	10.5
5.05	4.5	10.0
5.91	4.0	9.0
6.33	4.0	8.0
6.76	3.5	7.5
7.20	3.0	7.0

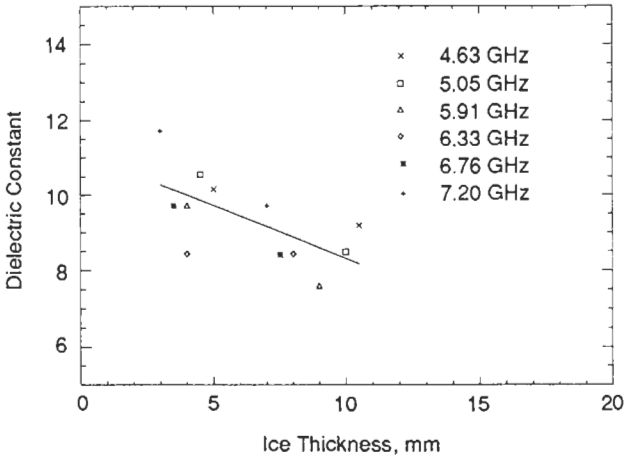

Fig. 9-15. Calculated dielectric constant as a function of the ice thickness.

9.4 UREA ICE

Urea ice is structurally identical to saline ice [Gow, 1984]. Under calm conditions it develops a columnar structure characterized by thin plates of pure ice that separate vertical planes of pockets filled with urea solution. Because urea is a covalent molecule, an urea solution is less conductive than brine. Nevertheless, at frequencies above 10 GHz and at temperatures near 0°C, the imaginary parts of the dielectric constant of saline water and even fresh water are identical [Ulaby et al., 1982, p. 2023]. The real part of the dielectric constant of saline water is a few percent less than that for fresh water. The complex permittivity of both fresh and saline water is strongly frequency dependent over 1 to 100 GHz.

Radar backscatter measurements of urea ice were acquired because urea is noncorrosive and, hence, large quantities can be easily managed in an indoor facility. Data were collected with 13.9 and 35 GHz polarimetric scatterometers during the growth and evolution of several urea ice sheets.

Normalized radar cross sections of smooth urea ice at different angles of incidence greater than 20° and at like and cross polarizations are shown in Figure 9-16 at 35 GHz. Figure 9-17 shows like-polarization cross sections at 13.9 GHz corrected for antenna beamwidth effects for both smooth urea ice and saline ice. Both figures show a strong, exponential decrease in cross section with increasing incidence angle although there is almost a 20 dB difference

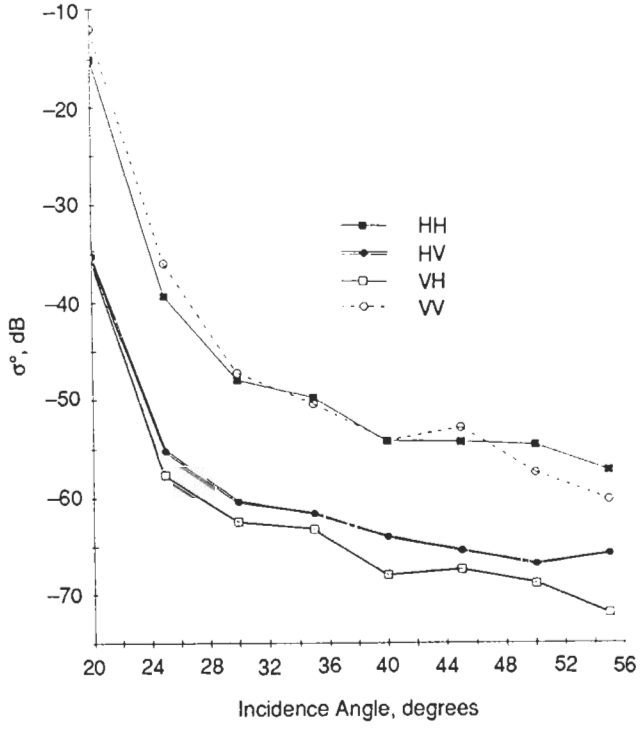

Fig. 9-16. Polarimetric normalized radar cross section (σ°) of smooth urea ice at 35 GHz [Colom, 1991].

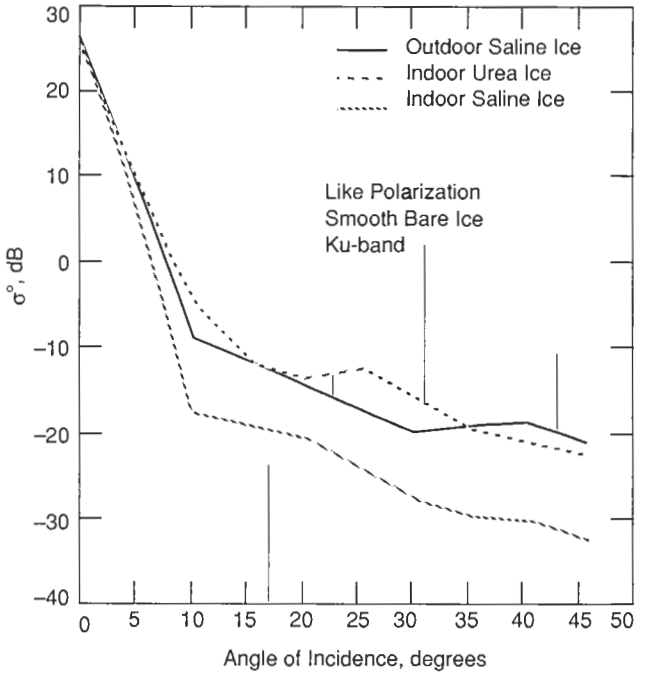

Figure 9-17. Beamwidth corrected backscatter coefficients for two saline ice sheets and an urea ice sheet. One of the saline sheets and the urea ice sheet were grown indoors. The second saline sheet was grown on an outdoor pond.

between the 13.9 and 35 GHz data at large angles at like polarization. Also at larger angles, the 13.9 GHz urea ice data are about 10 dB lower than those for saline ice, possibly because of the difference in dielectric constant between the two materials. Because the ice was smooth and there was no distinction between the HH- and VV-polarization components, any residual power at 13.9 GHz is attributable to volume scattering. The low power levels at large incidence angles indicate that the inclusions must be small compared to a wavelength.

An experiment was conducted to discriminate between surface and volume scattering. A smooth sheet of urea ice was grown indoors until it was 30.5 cm thick. The surface was smooth enough so that surface scattering was negligible. The temperature of the room was slowly raised over a period of 48 hours to observe any change in the resultant backscatter. It was anticipated that any changes could be primarily attributed to volume scattering. Figure 9-18(a) shows the results of this experiment at 35° and 45° of incidence where σ was plotted versus ice temperature. The trends shown are also consistent for each of the four polarizations plotted in Figure 9-18(b). As expected, σ is lower for a larger incidence angle. The value of σ is also low for the smooth ice at temperatures of approximately –9° and –8°C. The value of σ increases slowly until it reaches a maximum around –1°C and then drops off. During the experiment, air bubbles 2 to 5 mm wide were observed near the surface for a temperature range of –2° to 0°C. Bubbles formed because pockets of urea solution drained, leaving cavities partially or completely filled with air. The ice sheets free of

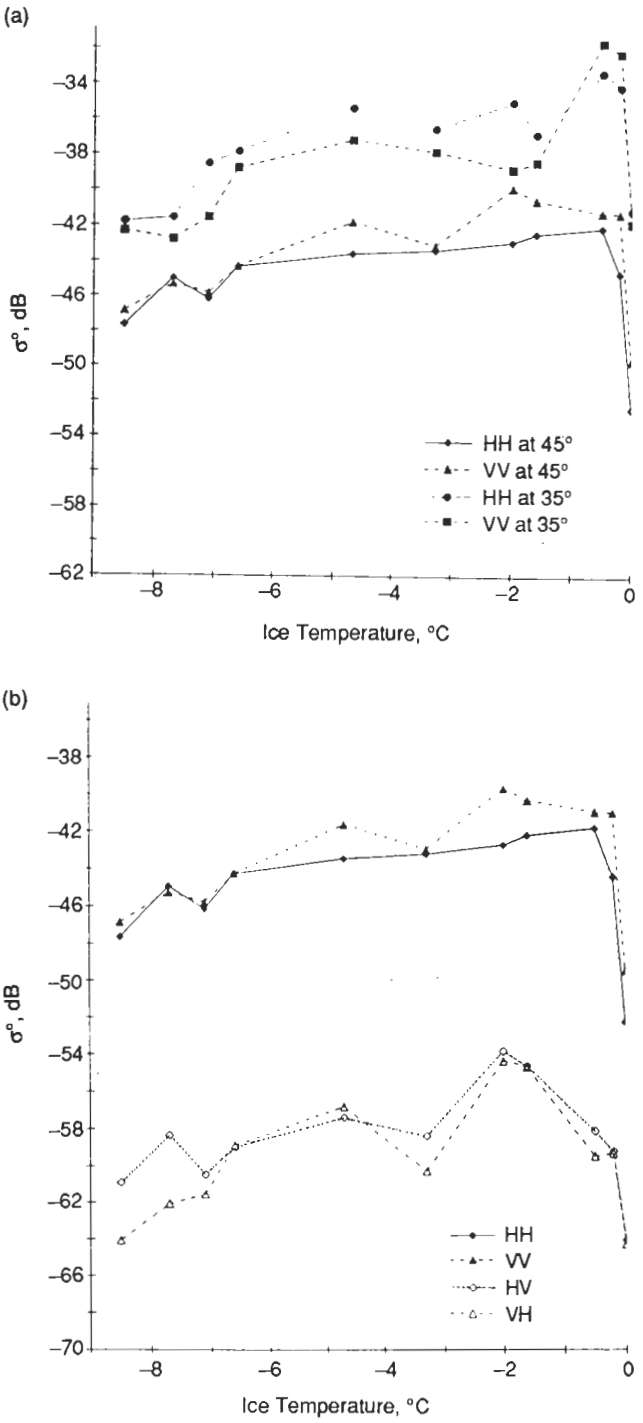

Fig. 9-18. Normalized radar cross section (σ°) versus ice temperature at (a) 35° and 45°, and (b) polarimetric cross sections at 45° [Colom, 1991].

an urea solution present low loss to the microwave signal, scattering more energy and explaining the maximum at about –1°C. Eventually, water filled the air pockets and covered the ice sheet, masking the scatterers located below the surface. Indeed, the scattered signal decreased considerably at 0°C.

9.5 DESALINATED ICE

Ice sheets were left in place on the outdoor pond at CRREL for up to several months. One ice sheet, grown in January 1988, grew to a thickness of 16 cm, at which point ice cubes were distributed on the surface to simulate roughness. The ice sheet was left undisturbed until late January when unseasonably warm air temperatures caused the surface to melt. Fresh water so formed flushed much of the brine from the ice sheet. Periods of growth and melt followed until late February, when the ice was about 31 cm thick. The salinity of the ice in the top 5 cm of the ice sheet was less than 0.5‰. The density in the top 10 cm of the ice was about 0.89 mg/m^3.

Measurements were made in 1989 on the desalinated ice blocks as mentioned in Section 9.2 [Gogineni, S. P., J. W. Bredow, A. J. Gow, T. C. Grenfell, and K. C. Jezek, Microwave measurements over desalinated ice under quasi-laboratory conditions, submitted to *IEEE Transactions on Geoscience and Remote Sensing,* 1992]. Salinities in the upper 5 cm were less than 1.0‰ with densities in the upper 10 cm varying between 0.84 and 0.87 mg/m^3. Ice characteristics from both the 1988 and 1989 experiments appear in Table 9-3.

TABLE 9-3. Ice surface and internal characteristics.

Year	RMS height, cm	Standard deviation, cm	Correlation length, cm
1988	0.18	0.07	2.5
1989	0.08	0.15	3.3

Year	Bubble size, mm	Correlation length, mm	Bulk density
1988	0.5	—	—
1989	0.45	1.5–2.0	0.844

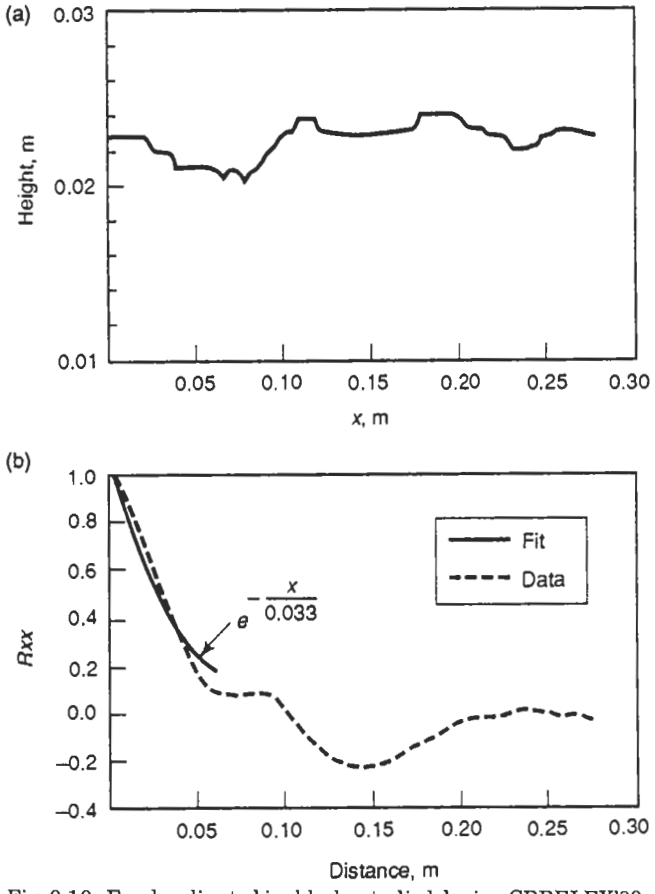

Fig. 9-19. For desalinated ice blocks studied during CRRELEX'89: (a) surface profiles, and (b) computed autocorrelations and minimum-mean-square-exponential fits.

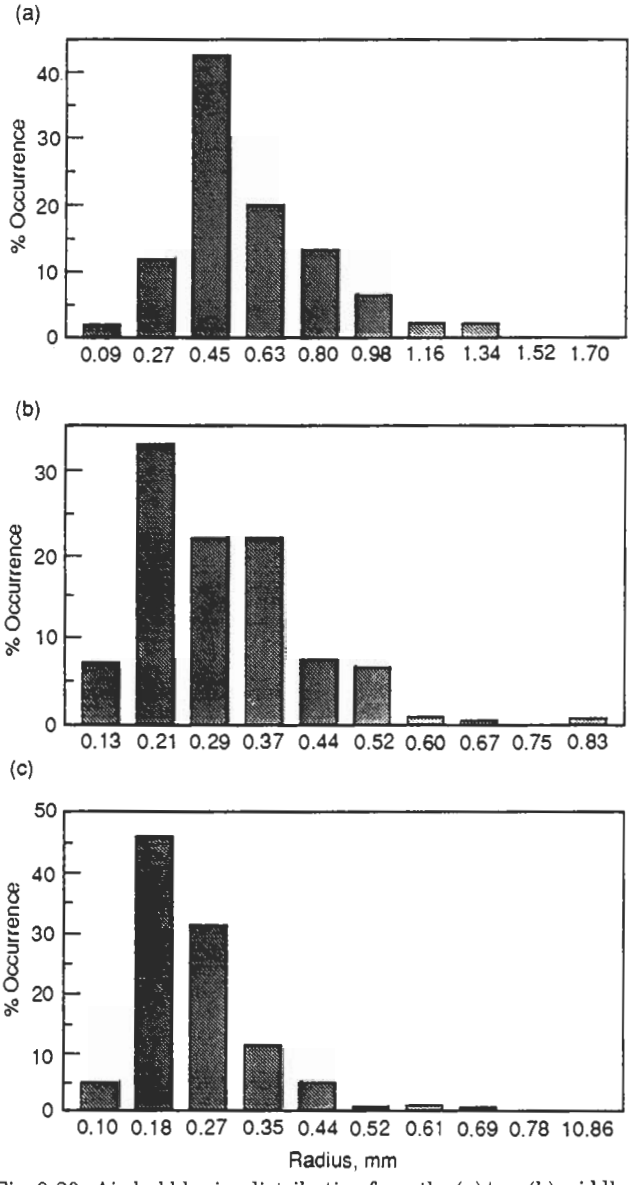

Fig. 9-20. Air-bubble size distribution from the (a) top, (b) middle, and (c) bottom of a block of desalinated ice studied during CRRELEX'89.

Figure 9-19(a) shows a typical surface roughness profile obtained using a contour gauge. The corresponding autocorrelation function is shown in Figure 9-19(b). Bubble size and distribution were determined from photographs of vertical and horizontal thin sections taken from the desalinated blocks. Bubbles were highlighted and the images digitized. Figure 9-20 shows a typical bubble distribution obtained from the desalinated ice.

Figure 9-21 shows the results of radar backscatter measurements made on the desalinated ice at C-band. The bars represent the total uncertainty in the scattering coefficient estimate resulting from random and systematic errors. The upper curve is the maximum value of σ obtained by increasing the rms height by one standard deviation and reducing the correlation length by one standard deviation. The minimum values of σ, represented by the lower dashed curve, were determined by decreasing the rms height by one standard deviation and increasing the correlation length by one standard deviation. The decay of σ with incidence angle is similar to that observed on saline ice. This decay indicates that surface scattering is the dominant source of scattering. To confirm this, data were collected over a 24-hour period to determine the temperature dependence of the scattering coefficient (Figure 9-22). At X-band, scattering from the ice sheet decreased by more than 10 dB when the ice temperature increased from about –5° to –3°C. There was negligible change at C-band. The decrease in scattering at X-band can be attributed to the presence of moisture on the surface, which reduced the volume contribution. However, because we did not observe a corresponding reduction at C-band, we concluded that scattering at C-band is dominated by the ice surface.

The dependence of emissivity on frequency and nadir angle are shown in Figure 9-23 for the desalinated ice measured during February 1988. The error bars indicate the standard deviation of the results of twelve sets of observations. The resulting frequency spectrum, Figure 9-23(a), shows a very weak frequency dependence. The emissivity spectra measured on the desalinated blocks created in 1989 show more structure (Figure 9-24). The maxima at 6 and 37 GHz are suggestive of interference fringes, however, the variation with incidence angle is quite weak (Figure 9-25). The differences between the 1988 and 1989 ice sheet simulations are pronounced. Removal of the blocks in 1989 no doubt allowed brine to drain from the entire slab. Low block salinities would have resulted in a decrease in the optical thickness of the ice. That the ice sheet was left in place in 1988, would suggest there was still substantial brine in the lower part of the ice slab. Higher salinities in the lower portion of the ice sheet could have caused sufficient attenuation to eliminate fringe effects.

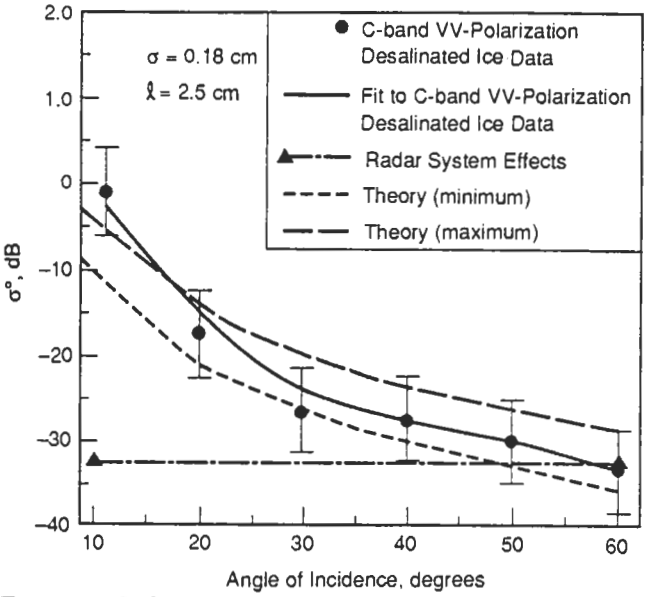

Fig. 9-21. Backscatter cross section of desalinated ice sheet at C-band, as determined from data obtained during CRRELEX'88, compared with predictions of the Small Perturbation Method.

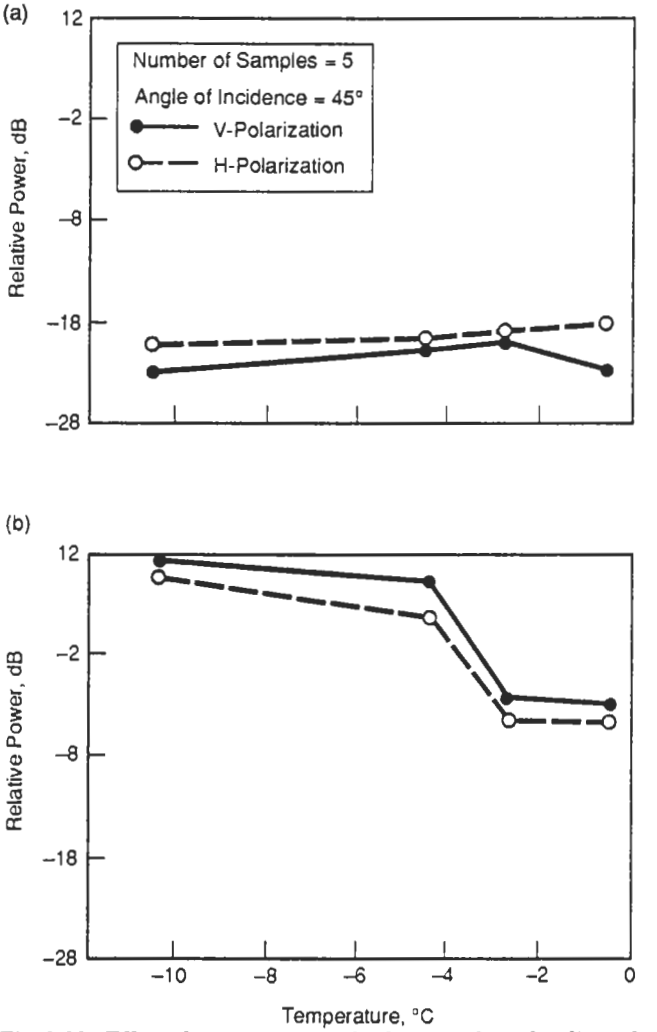

Fig. 9-22. Effect of temperature on backscatter from desalinated ice at (a) C-band and (b) X-band as determined from data obtained during CRRELEX'88.

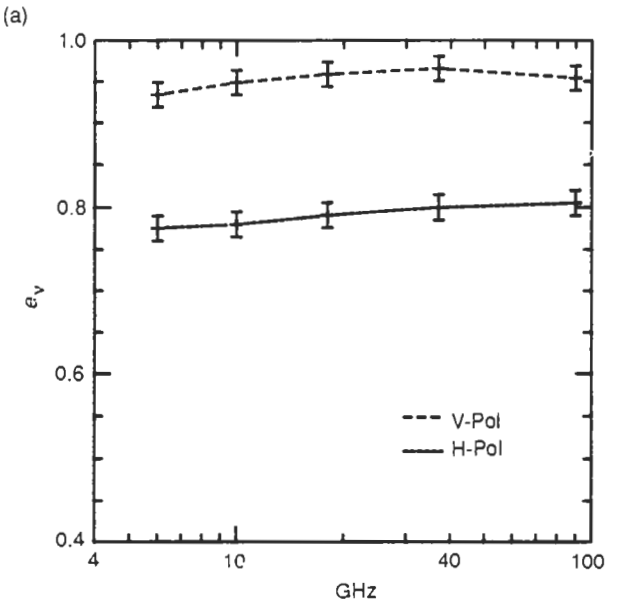

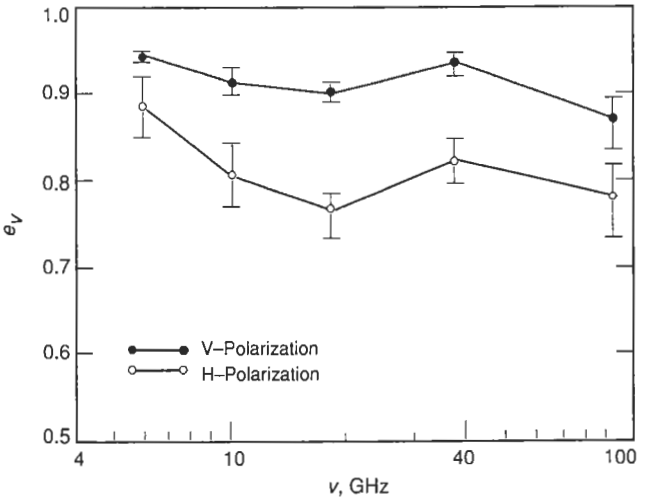

Fig. 9-24. Microwave emissivity versus frequency for the desalinated blocks in January 1989. The error bars denote the standard deviation for four independent samples.

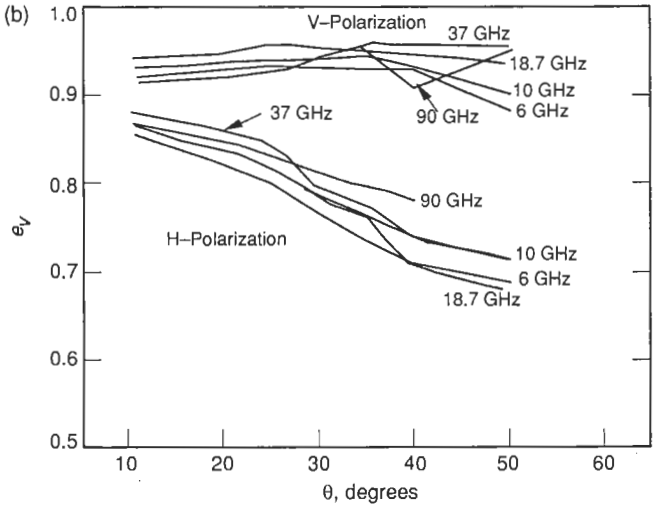

Fig. 9-23. (a) Emissivity spectra from 6 to 90 GHz of a desalinated ice sheet at V- and H-polarizations. (b) Microwave emissivity versus incidence angle for the desalinated pond ice. Curves give the results for the five observation frequencies.

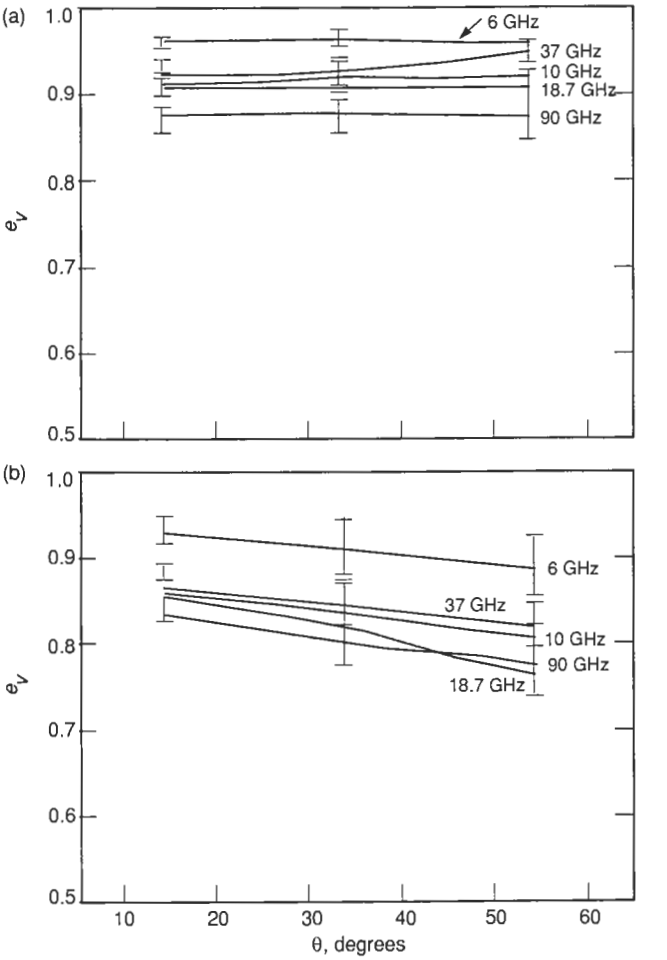

Fig. 9-25. Microwave emissivity versus incidence angle (a) V and (b) H polarizations for the desalinated blocks.

9.6 PANCAKE ICE

Pancake ice was simulated by installing a wave-generating paddle at one end of the outdoor pond. Pancakes were formed with thicknesses of about 7 cm. The surface emissivity increased as the ice froze, but never achieved the values previously recorded for congelation ice. C-band observations indicated that the increase in brightness temperature was linear with thickness, contrary to the nonlinear relationships discussed earlier. This linear variation existed because the brightness temperature was being modulated more strongly by varying concentrations of ice and slush–water. As time and thickness increased so could the concentration of ice, however no quantitative method

for estimating the relative percentage of ice and slush was available.

9.7 SURFACE EFFECTS

The vertical distribution of brine changes rapidly as the ice sheet grows from the melt. As evidenced by the above results, this early redistribution of brine and the formation of brine pockets within the ice has a primary influence on microwave signatures. As the ice sheet continues to age, secondary metamorphic processes begin to rework the surface. Natural processes such as mechanical deformation, frost flowers, and snow cover will each produce different but characteristic scales of surface roughness and near-surface inhomogeneities that modify, and may eventually dominate, the electromagnetic response.

Several types of surface processes were duplicated in the indoor and outdoor laboratories. Results of those experiments are discussed in the following sections.

9.7.1 Roughened Surface

A roughened ice sheet was simulated by mechanically raking and gouging the ice surface. This produced an irregular texture with 2- to 3-cm height variations. Figure 9-26 shows the angular dependence of the backscattering coefficient for smooth, rough, and snow-covered ice at 9.6 GHz (HH-polarization). Roughening causes the scattering coefficient to increase by about 10 dB over the results for smooth ice at incidence angles greater than 20°. The shape of the backscattering curve is indicative of surface scattering. However, a volume contribution may be comparable to the surface term at large incidence angles because a volume term must be included to model the scattering from smooth saline ice. Of course, as the surface gets rougher, the volume term becomes less and less important.

Radiometer data were collected on the same ice sheet. Before roughening, the ice sheet was optically thick and there was no clear dependence of emissivity on frequency and incidence angle at vertical polarization. At horizontal polarization, the undisturbed ice showed the usual frequency and incidence angle dependence [Grenfell and Comiso, 1986]. After roughening, all of the horizontal observations at 18 and 37 GHz showed a large increase in emissivity (Figure 9-27). For vertical polarization, the 10- and 90-GHz emissivities decreased while the 18-GHz emissivity increased at 40° and 50° incidence. The 37-GHz emissivity increased at 60°. Grenfell and Comiso [1986] argued that the results at 18 and 37 GHz were explained by the fact that the scale of roughness was close to the wavelengths at these frequencies. All other results were within the range of expected values from conventional scattering and emission theory of rough surfaces [Ulaby et al., 1982]. When the rough layer was scraped off, the emissivities decreased further, suggesting that a thin liquid skim had formed on the smooth surface.

9.7.2 Rubble Surface

A rubbled ice surface was created by spreading fresh ice chunks on top of an 8-cm thick ice sheet. At this thickness, the physical properties of the ice sheet are only slowly changing, so sequential microwave observations essentially view the same material. The ice sheet grown for this experiment was very smooth (0.05 cm rms) and was snow-free. Ice surface temperatures prior to application of the ice chunks were about –16°C. Warmer air temperatures later in the experiment and after the chunks were applied caused the ice surface temperature to rise to about –8°C. The rubble layer was about 2.5 cm thick and photographs of vertical thick sections are shown in Figure 9-28. Environmental descriptions of bare and rubble-covered ice sheets are listed in Table 9-4. The scale of roughness simulated here is similar to that observed for pancake ice. Roughnesses greater than this are usually associated with large-scale deformation processes (i.e., strewn blocks and rubble).

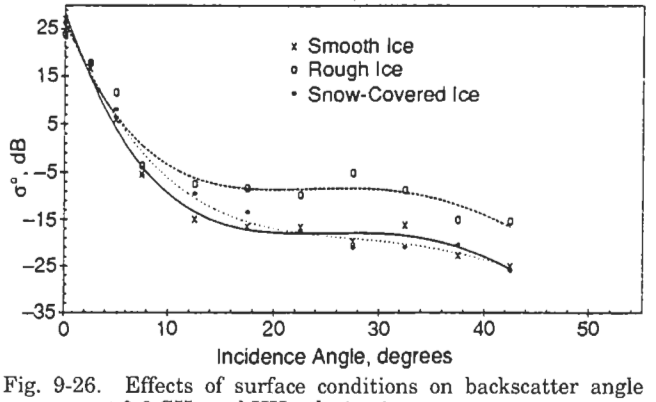

Fig. 9-26. Effects of surface conditions on backscatter angle response at 9.6 GHz and HH polarization.

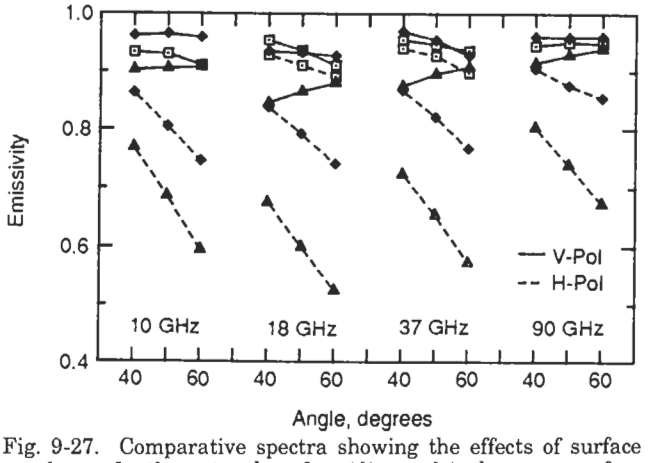

Fig. 9-27. Comparative spectra showing the effects of surface roughness for the natural surface (diamonds), the same surface after roughening (squares), and after the rough upper surface was scraped off (triangles) [Grenfell and Comiso, 1986].

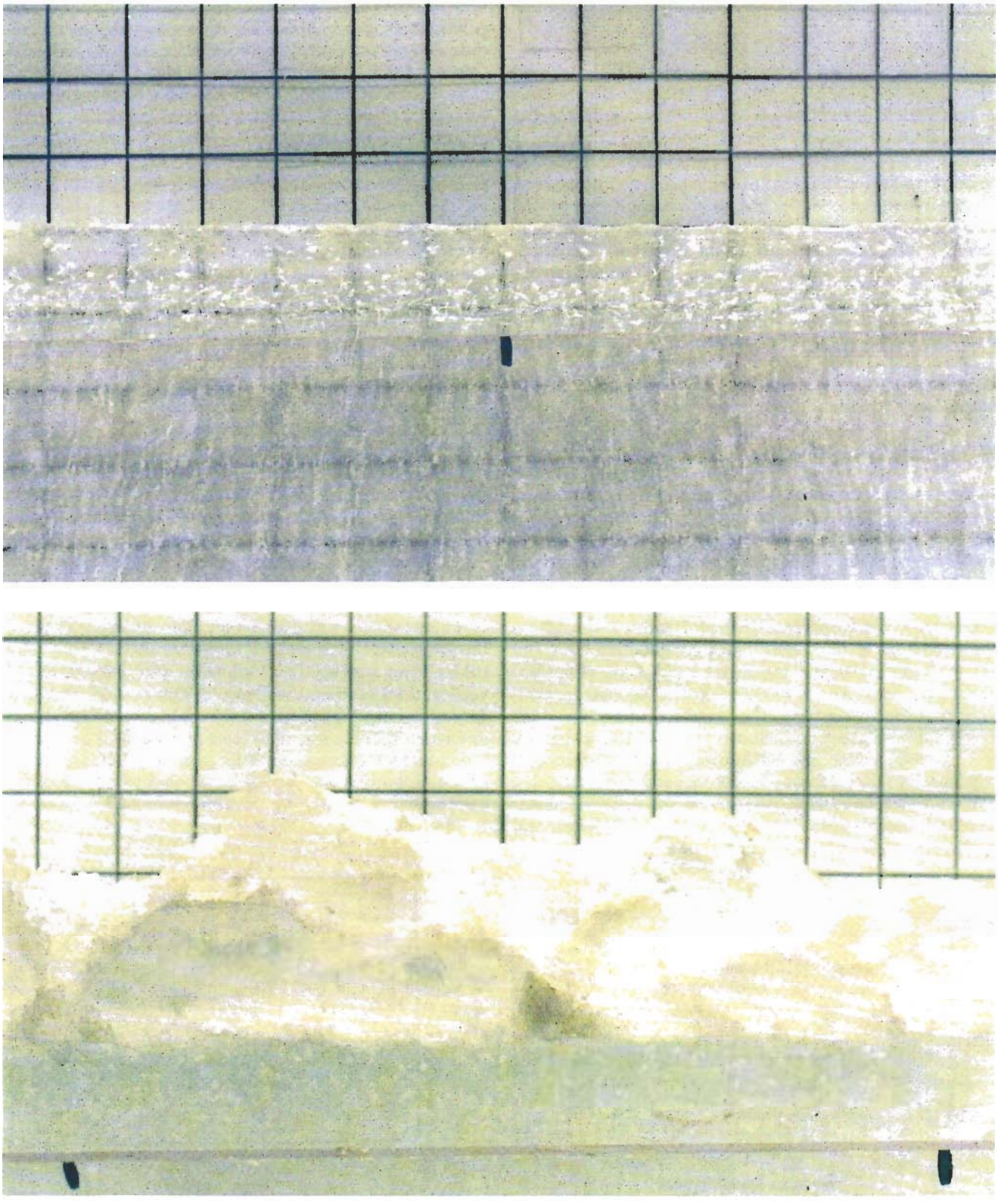

Fig. 9-28. Vertical thick sections showing the air–ice interface for (a) slightly rough and (b) very rough grey ice. The grid spacing is 1 cm.

TABLE 9-4. Summary of the physical property observations for a grey ice sheet with a smooth and rough surface [Onstott, 1990].

Description	Grey ice smooth	Grey ice rough
Ice age	70 hours	100 hours
Ice thickness	7.5 cm	8.3 cm
Snow cover	none	none
$\sigma_{roughness}$	0.048 cm rms	0.544±0.053 cm rms
$\ell_{correlation.length}$	0.669 cm	1.48 ±0.334 cm
T_{air}	–23.5 to –26.6°C	–14.6 to –18.1°C
T_{ice}	–16°C	–8°C
Bulk salinity	10.1‰	10.1‰ (ice sheet)
Top 5 cm		0 ‰ (roughness elements)

A few comments are necessary before presenting and comparing data. First the magnitude of the dielectric constant of bare ice is about twice that of fresh ice. Consequently, the backscatter cross sections from rough ice require an increase of about 3.7 dB to account for this difference. Relative to the radar wavelength, there is almost an order of magnitude change in surface roughness between the bare and rubble-covered ice sheets (Figure 9-29). At 5 GHz and like polarization, backscatter increases by about 19 dB at 40°, while at 10.0 GHz it increases about 22 dB after the surface has been roughened.

Passive microwave observations of the same scene yielded results similar to those reported earlier for raked surfaces. At 6 GHz and vertical polarization, the emissivity was constant before and after addition of the rubble layer. As shown in Figure 9-30, the emissivity decreased at the higher frequencies after the rubble was added. This response is likely explained by the fact that the rubble layer is rough at higher frequencies but smooth at C-band. Horizontal polarization observations showed that the emissivity at low frequencies rose slightly, but decreased at higher frequencies. As presented in Figure 9-31, the C-band data between 4.9 and 7.2 GHz included a maximum at the low frequency and a minimum at the high frequency, consistent with a first-order fringe pair from a 2-cm layer with a dielectric constant of 1.15.

A rubble layer was deposited on the surface of an urea ice sheet. Chunks of urea ice 2 to 5 cm square were spaced over a new, smooth urea ice sheet. Figure 9-32 shows backscatter coefficients for rough ice versus the angle of incidence. As expected, backscatter is stronger for this case than for the smooth ice case (Figure 9-16), especially at large incidence angles.

9.7.3 *Snow-Covered Surface*

Snow cover is ubiquitous over sea ice and can significantly affect the microwave backscatter or emissivity [Kim et al., 1984; Comiso et al., 1989]. Snow cover overtly modifies the electromagnetic signature of sea ice simply by addition of another layer of scattering particles. But the influence of snow cover on sea ice is also more subtle. Snow acts as an insulator and a mechanical load. This combination serves to release brine from just below the ice surface. The brine is subsequently wicked up into the snow layer [Grenfell and Comiso, 1986]. If the snow is thick enough, the load can be sufficient to depress the ice sheet below its natural freeboard, and flooding will occur. Several laboratory experiments were carried out to assess the effects of a snow cover over sea ice and the subsequent flooding and refreezing of a basal slush layer on active and passive microwave signatures.

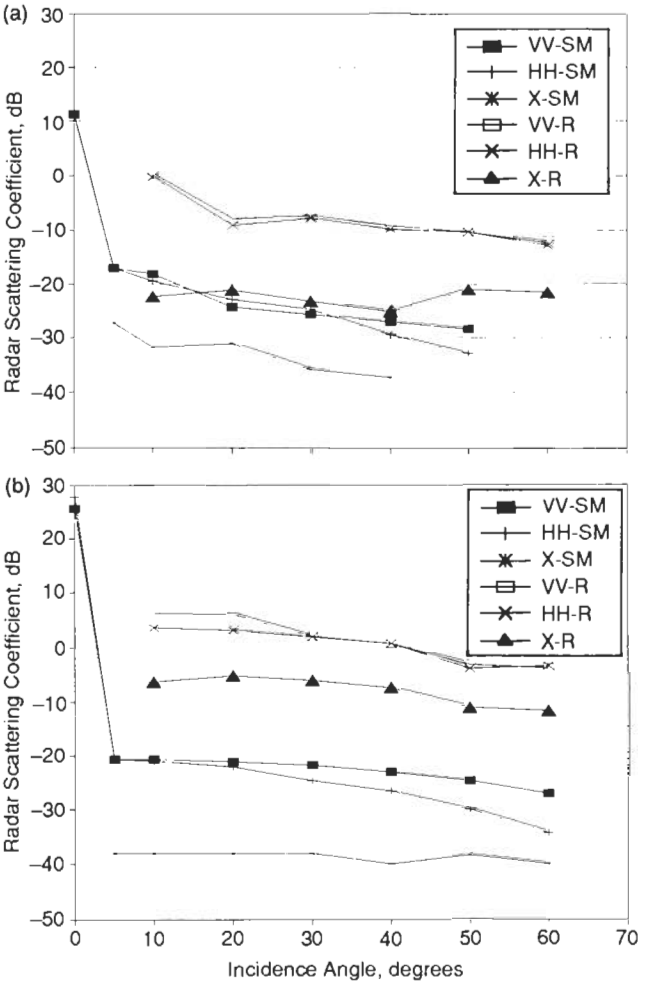

Fig. 9-29. Radar scattering coefficient response for ice with a rough (R) or smooth (SM) surface. The response is shown at (a) 5.0 and (b) 10.0 GHz.

Naturally falling, dry snow accumulated on a saline ice sheet grown on the outdoor pond. The snow layer reached a thickness of 4.5 cm. Snow-covered and smooth ice returns at 9.6 GHz were similar in magnitude, indicating that thin snow cover has negligible effect on backscattering from

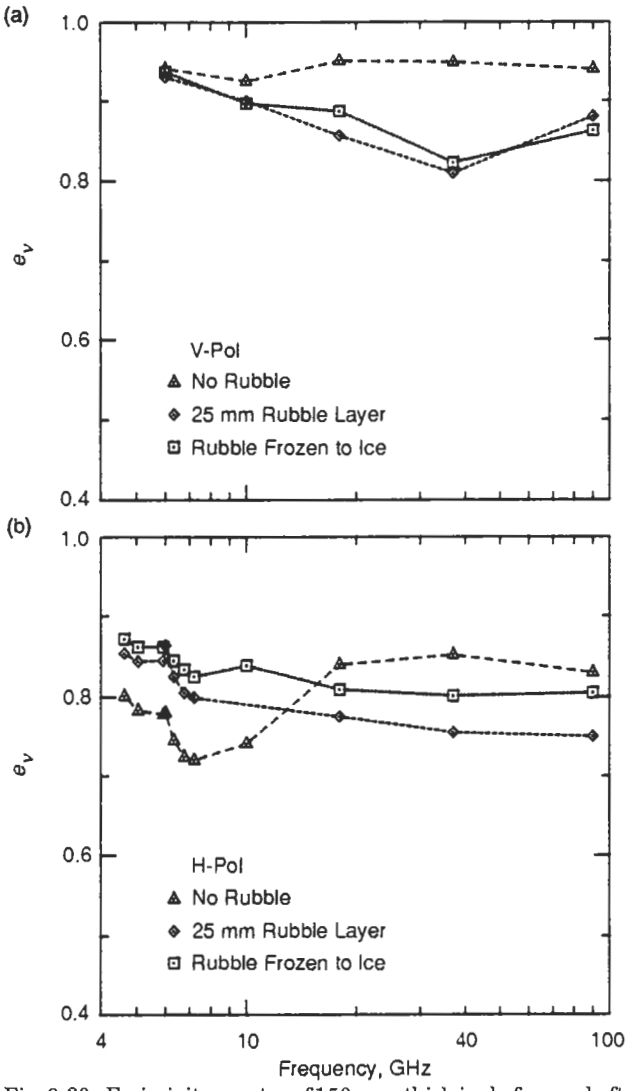

Fig. 9-30. Emissivity spectra of 150-mm-thick ice before and after the addition of a 25-mm layer of ice rubble at (a) vertical and (b) horizontal polarizations [Grenfell et al., 1988].

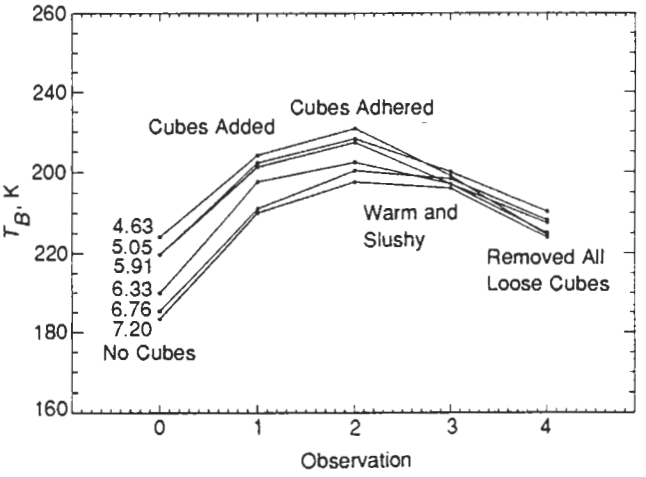

Fig. 9-31. C-band brightness temperature with varying surface roughness. Observation 1 was made immediately after adding approximately 2.5 cm of ice cubes to a 13.2-cm-thick ice sheet. Observation 2 was made the following morning, after most cubes had become frozen to the ice surface. Three hours later, the surface temperature had increased to –4°C for observation 3. Finally, for the last observation, the surface was raked to remove all loose cubes.

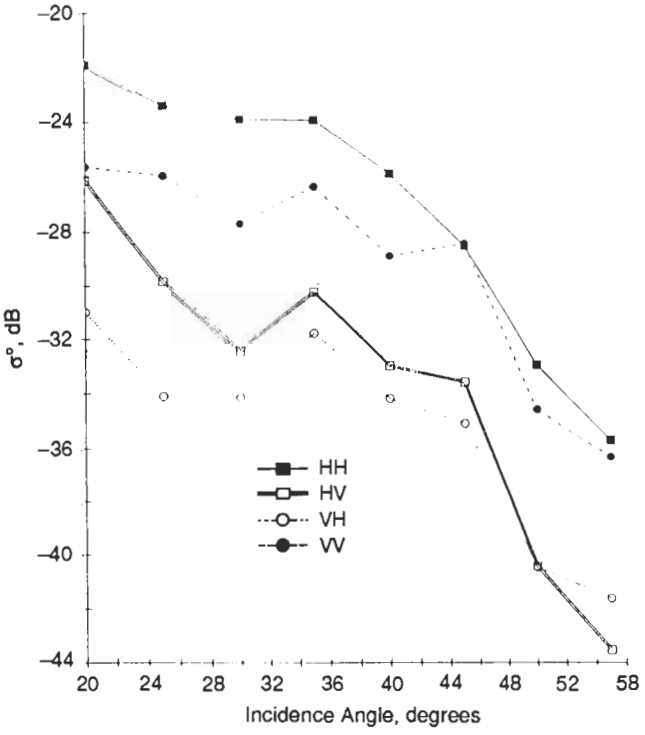

Fig. 9-32. Normalized radar cross section of rough ice at 35 GHz [Colom, 1991].

saline ice [Bredow, 1991]. However, backscatter coefficients of snow-covered ice at 13.6 GHz were about 3 dB higher than those of smooth ice at incidence angles greater than about 20° (Figure 9-33). Radiometer measurements of snow-covered saline ice recorded an increase in polarization and a decrease in emissivity, with a stronger decrease occurring at higher frequencies [Grenfell and Comiso, 1986]. Measurements at C-band (Figure 9-34) indicated the possibility of an interference effect, which, because of the snow depth, appeared to cause a spectral emissivity inversion to occur.

Lohanick [1992] conducted a series of detailed radiometric observations of snow-covered saline ice. Data were acquired at 10 and at 85 GHz before and for several weeks after a single snowfall event. A time series of 45° incidence-

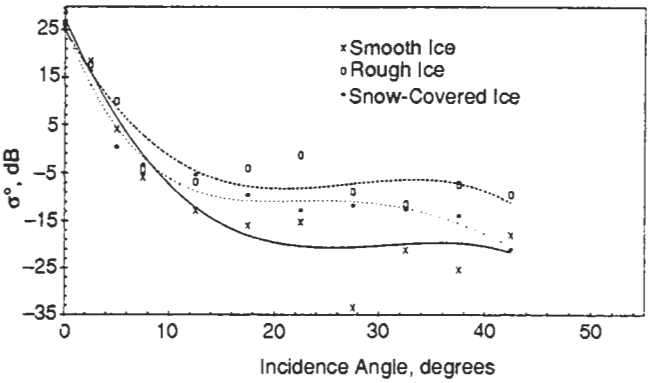

Fig. 9-33. Effects of surface conditions on backscatter angle response at 13.6 GHz and HH polarization.

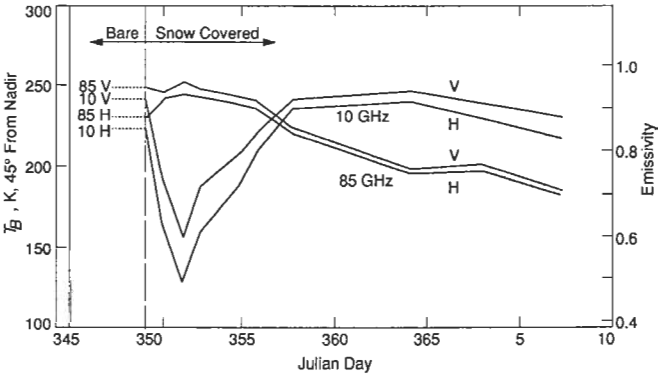

Fig. 9-35. Brightness temperatures and emissivities at 10 and 85 GHz and 45° incidence angle before and after the development of a snow cover on top of a saline ice sheet [Lohanick, 1992].

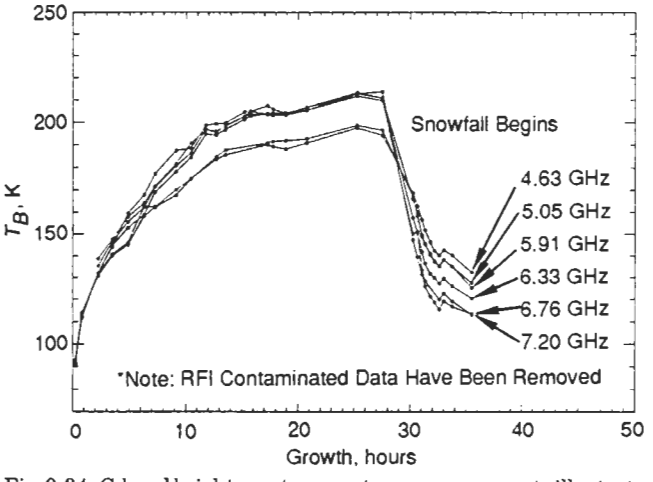

Fig. 9-34. C-band brightness temperature measurements illustrate the effect of light snowfall on a sheet of frazil ice. The snow thickness reached only 1 cm and became very moist over time.

angle radiometric temperature and emissivities for 10 and 85 GHz is shown in Figure 9-35. Snow fell late on Julian day 349. Dotted lines in Figure 9-35 show bare ice brightness temperatures. Emissivities at 10 GHz were calculated by dividing the brightness temperature by 268 K, the measured ice surface temperature; 85-GHz emissivities were calculated by dividing brightness temperature by snow surface physical temperature.

Figure 9-35 shows a significant drop (100 K) in 10-GHz brightness temperatures after snow deposition. Lohanick [1992] argued that the formation of a slush layer at the base of the snow was responsible for the behavior of the low frequency data. Brine wicked upwards into the snow caused a slush layer to form. This layer behaved radiometrically as a rough water interface. As the layer froze, it evolved to look more like water-saturated snow and finally a near perfect emitter at 10 GHz.

The 85-GHz data apparently were affected only by the snow layer. The 85-GHz brightness temperatures slowly dropped during the experiment and its polarization remained constant. This suggested an explanation relying on increased volume scatter in the snow due to increased snow grain size.

A similar sequence of observations was made on urea and saline ice sheets growing in an indoor laboratory [Lytle, V. I., K. C. Jezek, R. Hosseinmostafa, and S. P. Gogineni, Laboratory backscatter measurements over urea ice with a snow cover at Ku-band, submitted to *IEEE Transactions on Geoscience and Remote Sensing*]. The 13.9-GHz radar backscatter observations were acquired during the growth phase and until the ice was approximately 9 cm thick (Figure 9-36). At that point, snow previously stored in a cold room was applied in three successive layers. Events 22, 23, and 24 represent the addition of three layers of snow that in total were 6.3, 11.2, and 14.8 cm thick, respectively. Event 25 represents the moment at which the snow-covered ice was freed from the restraining walls of the tank and began to flood. Event 35 represents the point at which the flooded snow layer was refrozen. Ice growth to 9 cm took about three days. The snow experiments, including flooding, were distributed over about 12 hours. The refrozen slush was measured about 15 hours after the intial flooding event.

As with the outdoor experiments, the snow caused the nadir return to decrease by about 4 dB, while oblique incidence returns increased by about 10 dB. Backscatter coefficients were essentially invariant with the thickness of the snow layer, which varied from 6 to 15 cm. Lytle and coworkers concluded that these observations could not be explained by volume scattering effects. Instead, and as concluded by Lohanick [1992], they attributed the observations to a metamorphosis of the snow–ice interface that caused additional surface scattering. The lower portion of the snow pack was observed to be wet because of the wicking phenomenon described earlier. Using a Kirchoff model, they found that an effective interface roughness of about 0.5 cm rms and a correlation length of 15 cm explained the observations.

After a 15-cm thick snow layer was applied to the ice surface, the section of the ice sheet covered with snow was freed from the restraining walls of the tank. The ice surface

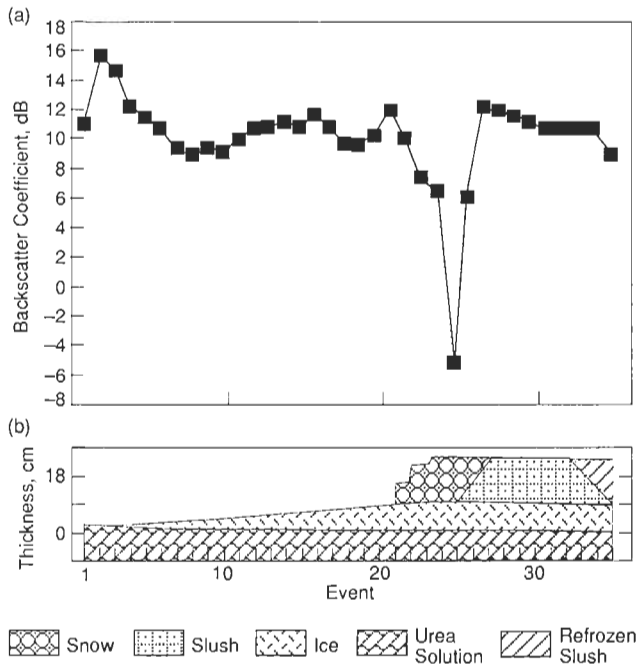

Fig. 9-36. (a) Evolution of backscatter coefficient with successive, controlled changes in ice sheet properties. Data were collected with a 13.9-GHz radar operating at normal incidence over an indoor tank filled with an urea solution. (b) The initial formation of ice from the melt (event 1) through the point at which the ice was about 9 cm thick (event 21) is shown. Events 22, 23 and 24 represent the addition of three snow layers. Event 25 represents the moment at which flooding begins.

depressed below the water level and the snow layer quickly flooded with urea solution. The entire column of snow eventually saturated with liquid. As soon as flooding occurred, normal incidence backscatter decreased by about 11 dB, but then rapidly increased to a level about 4 dB higher than backscatter measured prior to flooding. At 20° incidence angle, backscatter remained constant as the slush layer started to form; as the snow layer saturated the backscatter increased by about 5 dB. Increase in backscatter at all angles was attributed to the increased reflection coefficient at the flooded interface. Upon refreezing, backscatter at 20° incidence angle decreased 5 dB, similar to the level associated with an unflooded snow layer. This similarity was not unexpected. Although the overlying snow had been replaced by refrozen slush, the physical characteristics of this surface were expected to be similar to the ice–snow surface before flooding occurred.

Similar results have been derived from indoor laboratory measurements of snow-covered saline ice, and all observations are summarized in Figures 9-37(a), (b), and (c). These figures show that the backscatter coefficient consistently decreases at nadir with the application of a snow layer. They also show a consistent increase at oblique angles of incidence. Figures 9-38(a), (b), and (c) support the argument that interface roughness rather than volume scattering is the explanation for these data. These figures show the time domain response at 13.9 GHz over bare and snow-

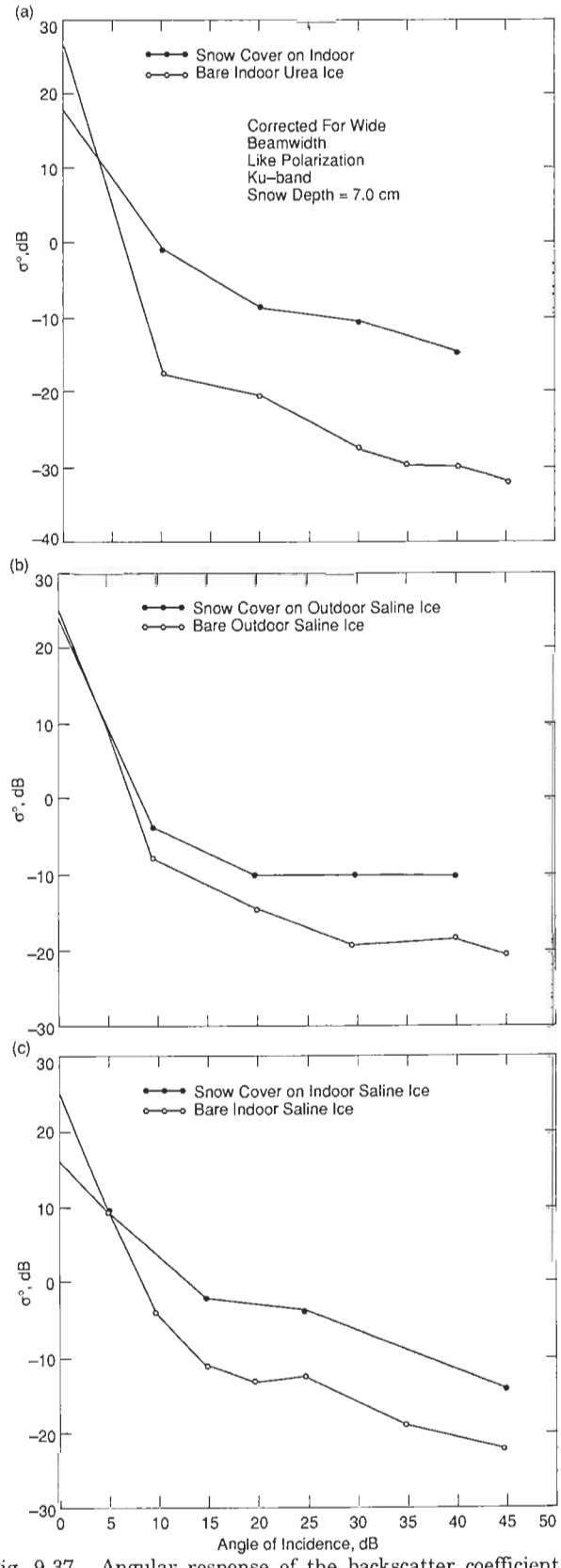

Fig. 9-37. Angular response of the backscatter coefficient at 13.9 GHz for three different bare and then snow-covered ice sheets: (a) urea grown indoors; (b) saline grown outdoors; and (c) saline grown indoors.

covered saline ice. The nadir signal from the ice surface is the large peak near the far left-hand side of Figure 9-38(a). Notice that application of a snow layer decreases the magnitude of the response, but application of additional snow does not change the pulse amplitude. Also there is no noticeable pulse broadening. At 45° incidence angle, the snow-covered return is about 10 dB higher than the equivalent bare ice result.

9.8 SIGNIFICANCE OF CRRELEX RESULTS

Experiments using the outdoor and indoor test facilities at CRREL demonstrated that saline ice with a predefined range of physical properties can be grown. These saline ice types include thin ice with varying crystalline textures and salinity gradients, roughened ice that includes a range of roughness elements, desalinated ice, and snow-covered ice. That selected ice properties can be isolated, duplicated, and studied in the laboratory is an important achievement. This achievement has been exploited to better understand the relationship between particular saline ice properties and microwave propagation phenomena. For example, there is excellent agreement between the dielectric constant of thin ice as determined from radar backscatter, radar transmission, and microwave emission observations. Moreover, changes in the dielectric constant are clearly seen to be related to the complex distribution of brine and the migration of brine through the ice sheet as the ice ages. Similarly, snow cover was found to have a profound effect on both active and passive microwave observations. Again, multisensor data could be interpreted consistently in terms of the dielectrically rough, slushy layer that develops at the snow–ice interface.

The unique combination of attributes that were part of CRRELEX makes it seem unlikely that equivalent insight into the specific microwave properties of saline ice could be obtained from field observations alone. Many of these new insights are very exciting, still, interpretation must be tempered by the broader objective of studying sea ice growing on the polar oceans. Growth in the natural ocean environment occurs under the influence of many competing effects. In turn, these effects integrate to yield a complex physical structure and associated microwave response. This natural integration reveals the basic limitation of CRRELEX, namely, that it is difficult, perhaps impossible, to simulate simultaneously all the processes that drive the formation of natural sea ice. For example, while desalinated ice of a particular composition could be grown in the laboratory, experimental techniques are far from duplicating the complete properties of even first-year ice. The CRRELEX experiences have established a new methodology for combining laboratory research that tests specific hypotheses using field measurements to evaluate the significance of a particular phenomenon in a complex environment.

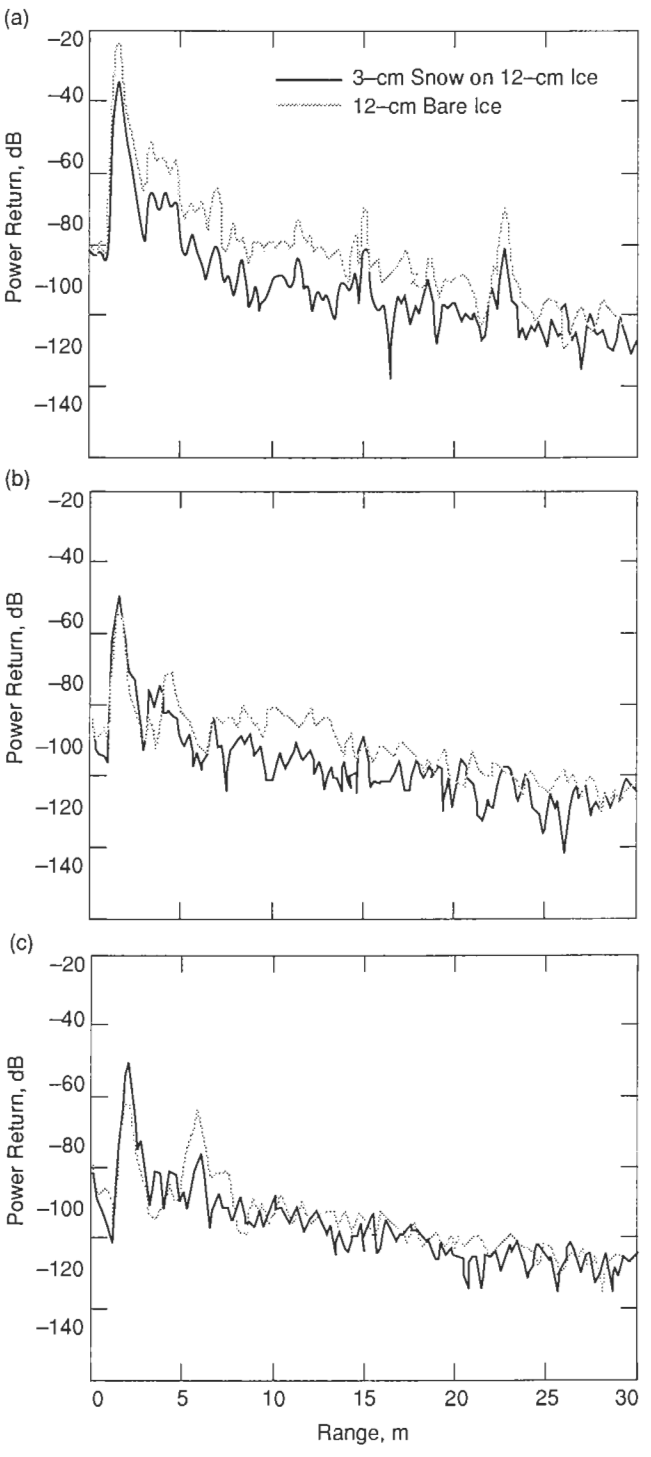

Fig. 9-38. Time domain response for a 13.9-GHz radar over bare and snow-covered saline ice. (a) The nadir signal from the ice surface corresponds to the large peak near the far left side. At (b) 25° and (c) 45° incidence angles, the backscattered signal with a slight time delay at oblique incidence also appears on the left side of each figure.

REFERENCES

Apinis, J. J. and W. H. Peake, *Passive Microwave Mapping of Ice Thickness*, Ohio State University Electrosciences Report 3892-2, Columbus, OH, 1976.

Arcone, S. A., A. J. Gow, and S. McGrew, Microwave dielectric structural and salinity properties of simulated sea ice, *IEEE Transactions on Geoscience and Remote Sensing, GE-24(6)*, pp. 832–839, 1986.

Bredow, J. W., *A Laboratory Investigation Into Microwave Backscattering From Sea Ice*, University of Kansas, Lawrence, Kansas, 173 pp., 1991.

Colom, J. G., *Development of a 35-GHz Network Analyzer Based Polarimetric Scatterometer*, University of Massachusetts, Amherst, Massachusetts, 107 pp., 1991.

Comiso, J. C., T. C. Grenfell, D. L. Bell, M. A. Lange and S. F. Ackley, Passive microwave in situ observations of winter Weddell sea ice, *Journal of Geophysical Research, 94(C8)*, pp. 10,891–10,905, 1989.

Gogineni, S. P., R. K. Moore, P. Wang, A. J. Gow, and R. G. Onstott, Radar backscatter over saline ice, *International Journal of Remote Sensing, 11(4)*, pp. 603–615, 1990.

Gow, A. J., *Crystalline Structure of Urea Ice Sheet Used in Modelling Experiments in the CRREL Test Basin*, CRREL Report CR84-24, CRREL, Hanover, New Hampshire, 1984.

Gow, A. J., W. Tucker, and W. Weeks, *Physical properties of summer sea ice in the Fram Strait, June–July*, CRREL Report 87-16, U.S. Army Cold Regions Research and Engineering Laboratory, Hanover, New Hampshire, 1987.

Grenfell, T. C. and J. C. Comiso, Multifrequency passive microwave observations of first year sea ice grown in a tank, *IEEE Transactions on Geoscience and Remote Sensing, GE-24*, pp. 826–831, 1986.

Jezek, K. C., T. K. Stanton, A. J. Gow and M. A. Lange, Influence of environmental conditions on acoustical properties of sea ice, *Journal of the Acoustical Society of America, 88(4)*, 1903–1912, 1990.

Kim, Y.–S., R. G. Onstott, and R. K. Moore, The effect of a snow cover on microwave backscatter from sea ice, *IEEE Journal of Oceanic Engineering, OE-9(5)*, pp. 383–388, 1984.

Kovacs, A., R. M. Morey, G. F. N. Cox, and N. C. Valleau, *Modelling the Electromagnetic Property Trends in Sea Ice and Example Impulse Radar and Frequency Domain Electromagnetic Ice Thickness Sounding Results*, Technical Report, CRREL, Hanover, New Hampshire, 1986.

Lohanick, A. W., Microwave brightness temperatures of laboratory grown undeformed first-year ice with an evolving snow cover, *Journal of Geophysical Research*, in press, 1992.

Onstott, R. G., *Active Microwave Observations of the Formation Process of Simulated Sea Ice,* Technical Report 239500-2-T, Environmental Research Institute of Michigan, Ann Arbor, Michigan, 1991.

Parkinson, C. L., J. C. Comiso, H. J. Zwally, D. J. Cavalieri, P. Gloersen, and W. J. Campbell, *Arctic sea ice, 1973–1976: Satellite passive-microwave observations*, NASA SP-489, 296 pp., National Aeronautics and Space Administration, Washington, DC, 1987.

Perovich, D. and A. J. Gow, A statistical description of the microstructure of young sea ice, *Journal of Geophysical Research, 96*, 16,943–16,953, 1991.

Stanton, T. K., K. C. Jezek, and A. J. Gow, Acoustical reflection and scattering from the underside of laboratory grown sea ice: Measurements and predictions, *Journal of the Acoustical Society of America, 80*, 1486–1494, 1986.

Swift C. T. and D. J. Cavalieri, Passive microwave remote sensing for sea ice research, *Eos, Transactions of the American Geophysical Union, 66*, 1210–1212, 1985.

Swift, C. T., D. C. Dehority, and A. B. Tanner, Passive microwave spectral emission from saline ice at C-band during the growth phase, *IEEE Transactions on Geoscience and Remote Sensing, GE-24(6)*, pp. 840–848, 1986.

Ulaby, F. T., R. K. Moore, and A. K. Fung, *Microwave Remote Sensing—Active and Passive, Vol. II: Radar Remote Sensing and Surface Scattering and Emission Theory*, Addison–Wesley Publishing Company, Reading, Massachusetts, 1982.

Zwally, H. J., J. C. Comiso, C. L. Parkinson, W. J. Campbell, F. D. Carsey, and P. Gloersen, *Antarctic Sea Ice, 1973–1976: Satellite Passive-Microwave Observations,* 206 pp., NASA SP-459, National Aeronautics and Space Administration, Washington, DC, 1983.